universe

Article

Release Episodes of Electrons and Protons in Solar Energetic Particle Events

Vasilis Kolympiris [1], Athanasios Papaioannou [2,*], Athanasios Kouloumvakos [3], Ioannis A. Daglis [1,4] and Anastasios Anastasiadis [2]

1 Department of Physics, National and Kapodistrian University of Athens, 15784 Athens, Greece
2 Institute for Astronomy, Astrophysics, Space Applications and Remote Sensing (IAASARS), National Observatory of Athens, I. Metaxa & Vas. Pavlou St., 15236 Penteli, Greece
3 The Johns Hopkins University Applied Physics Laboratory, 11101 Johns Hopkins Road, Laurel, MD 20723, USA
4 Hellenic Space Center, 15231 Athens, Greece
* Correspondence: atpapaio@astro.noa.gr; Tel.: +30-210-3490-882

Abstract: We analyzed a sample of 21 solar energetic particle (SEP) events with clear signatures in both near-relativistic electrons and high-energy protons spanning over ∼2.5 solar cycles from 1997 to 2016. We employed velocity dispersion analysis (VDA) for protons and fractional VDA (FVDA) for electrons, as well as time shifting analysis (TSA) in order to identify the solar release times (SRTs) of the electrons. We found that, for the majority of the events (62%), a simultaneous release was observed, while, for 14% of the events, electrons were released later than protons (i.e., delayed electrons); for 24% of the events, the opposite result was found (i.e., delayed protons). We found that the path length (L) traveled by the protons and electrons was not related to the aforementioned categorization. Moreover, we show that, in the case of simultaneous SEP events, protons and electrons are being released in close connection to type III and type II bursts, while the opposite is the case for delayed events. In addition, we demonstrate that, for the simultaneous events, both the proton and the electron release are established in heights $< 5R_S$ and that, especially for the well-connected simultaneous events, there is a co-occurrence of the type II burst with the release time of the particles.

Keywords: solar energetic particles (protons, electrons); radio bursts; solar flares; coronal mass ejections; shocks

check for updates

Citation: Kolympiris, V.; Papaioannou, A.; Kouloumvakos, A.; Daglis, I.A.; Anastasiadis, A. Release Episodes of Electrons and Protons in Solar Energetic Particle Events. *Universe* **2023**, *9*, 432. https://doi.org/10.3390/universe9100432

Academic Editor: Xueshang Feng

Received: 27 February 2023
Revised: 18 September 2023
Accepted: 23 September 2023
Published: 27 September 2023

1. Introduction

Solar energetic particles (SEPs) are accelerated at the Sun or in the interplanetary (IP) medium during eruptive solar events such as solar flares and coronal mass ejections (CMEs). Once the particles are injected onto open magnetic field lines, they propagate along the interplanetary magnetic field (IMF) from the Sun to the Earth. SEPs can reach energies spanning from a few keV to a few GeV [1]. A dichotomous distinction between the "impulsive" and "gradual" classes of SEP events [2] indicates the following: (a) "impulsive" events originate in the low corona due to magnetic reconnection, are short in duration, reach lower peak fluxes, and are associated with solar flares and type III radio bursts; (b) "gradual" SEPs are characterized by longer durations, larger peak intensities, are associated with CMEs and type II radio bursts, and originate higher in the corona when the CMEs are able to form a shock that will efficiently accelerate the particles [3]. Nonetheless, this dichotomous scenario is considered to be an oversimplification and is challenged by observations (see, e.g., [4,5]). Many studies searched for a preferential correlation between the parameters describing the importance of SEPs on the one hand and the eruptive solar activity on the other [6]. Results indicate that comparable correlations have been obtained with the CME speed (i.e., they are indicative for fostering a shock) and with soft X-ray (SXR) peak fluxes (i.e., they are indicative of the flare strength), which fail to point to a single dominant accelerator. This pitfall was first indicated by Kahler [7] who proposed the "big flare syndrome", thereby highlighting the fact that solar activity parameters (i.e., the flare strength and CME speed, for instance) are intercorrelated. Building on this, sophisticated statistical methods were used to further demonstrate that (for example) SEP peak intensities are indeed significantly correlated with both the CME speed and with flare parameters [8], especially with solar flare fluence [8,9]. These findings argue in favor of a mixed scenario, where processes related with both flares and CMEs contribute to SEP acceleration [4,6]. Moving forward, the dichotomous distinction was further challenged when a dependence on the energy of the SEPs was introduced [10]. In particular, energies < 20 MeV in SEP peak intensities had a higher correlation coefficient with CME speeds, while, for SEPs at energies > 20 Mev, the peak SEP intensities had a higher correlation coefficient with the flare peak photon flux, w hich is evidence of a mixed acceleration scenario where different acceleration processes dominate at different SEP energies. Moreover, in a detailed study of the large SEP event on 10 September 2017, multiple sources of high-energy protons were revealed [11].

Type III radio bursts emerge from electrons that are accelerated in processes associated with solar flares, wherein they propagate along open magnetic field lines outward from the Sun [12]. Those are associated with "impulsive" SEPs, but, more importantly, type III bursts provide direct observational evidence of the opening of the magnetic field lines, which is a prerequisite for the escape of particles into field lines that magnetically connect them to the observer [13]. Moreover, type II radio bursts are associated with electron beams accelerated at shock waves and usually with "gradual" SEP events [14] when a significant solar event takes place. These radio bursts are tracers of an evolving/travelling shock from low in the corona into the IP medium [3,15–17]. Furthermore, shock acceleration is most efficient at heights above $\sim$3 R_S. A prime set of SEPs that are accelerated to near-relativistic energies ($\geq$500 MeV) reach the Earth's atmosphere and trigger a cascade that results in secondary particles being recorded at the ground as enhancements above the background of the ever-present galactic cosmic rays (GCRs), which are called ground-level enhancements (GLEs; [18]). For GLEs, the inferred solar release time (SRT) was found to occur after the onset of the metric type II radio emission [2]. Additionally, when Reames [2] considered GLEs that were well connected (i.e., >W30°, thus establishing an optimal magnetic connection of the source site to the observer) their inferred release began at a shock height ranging between 2–4 R_S. This finding was later verified by an independent study [19] that reported a maximum of the release heights of high-energy protons at 3–4 R_S.

In order to shed light on the acceleration and release of protons and electrons in SEP events, Krucker and Lin [20] proposed two classes of events by utilizing the measurements of electrons (0.27–0.517 MeV) and ions (0.03–6 MeV) from the Wind/3DP [21]. In particular, in the first class, both the protons and electrons had the same path length (L), ranging close to the nominal Archimedian/Parker spiral ($\sim$1.2 AU), while, in the second class, the protons had a larger L (around 2 AU). Based on the time difference of the inferred release of the particles, these authors, assuming CME-driven shock acceleration, concluded that protons are accelerated higher than electrons in the corona in the first class and that protons exhibit a later release in the second class. Building on this, Kouloumvakos et al. [19] used ion measurements from the Solar and Heliospheric Observatory (SOHO)/Energetic and Relativistic Nuclei and Electron experiment (ERNE; [22]) (1.58–131 MeV) and electron recordings from the Wind/3DP (0.020–0.646 MeV), and they showed that, in half of the SEP events, the protons and electrons were released simultaneously, but, in the other half, the electron release was delayed compared to the proton release (on average by $\sim$7 min). They also showed that there is no clear-cut inference of the ordering relation between type III bursts and the release of protons and electrons. Nonetheless, Xie et al. [23], utilized SOHO/ *Electron Proton and Helium Instrument* (EPHIN; [24]) electron fluxes (0.25–10.4 MeV), SOHO/ERNE proton fluxes (13.8–101 MeV), and similar energy channels of the Solar and Terrestrial Relations Observatory (STEREO)/ Solar Electron Proton Telescope (SEPT; [25]), the High Energy Telescope (HET; [26]) and Low Energy Telescope (LET; [27]) detectors, wherein they demonstrated that near-relativistic electrons and high-energy protons are preferentially released simultaneously (within ±8 min) and explained the observed delays (when present) to transport effects and/or to the time necessary for the evolving shock to become strong enough to efficiently accelerate particles. In a follow up study, Ameri et al. [28] examined the release of the protons and electrons in SEPs using the SOHO/ERNE proton measurements (13.8–80.3 MeV) and the Wind/3DP electron measurements (0.06–0.646 MeV). They separated the events with respect to their release times and the onset of type II bursts with one category, including all the events with a release time before the onset of the type II bursts and a second category including all the events with a release at or after the occurrence of the type II burst. These authors concluded that the protons in the latter category of events were accelerated high in the corona, presumably in CME-driven shocks. They further noted that, provided that the protons in the former category were also accelerated by CME-driven shocks, the acceleration occurred low in the corona in that category of events. Nonetheless, for this case, they did not exclude accelerations below the heights of the CME leading front, in flares, or in CME-initiation-related processes. Moreover, Ameri et al. [28] found that most events demonstrate the simultaneous (within ±7 min) release of protons and electrons, while, in the rest of the events, they identified delayed proton release with respect to the electron release and an exception of one event for which the situation was directly opposite (i.e., the electrons were released later than the protons).

In this work, we investigated a sample of 21 SEPs that were clearly identified in both near-relativistic electrons and high-energy proton measurements, being further temporally associated. We employed velocity dispersion analysis (VDA) at protons ranging from 5–200 MeV, fractional VDA (FVDA) to electrons ranging from 0.020–0.646 MeV electrons, and time shifting analysis (TSA) to electrons ranging from 0.18–0.31 MeV (Section 2). Consequently, we compared the release times of the protons and electrons, and we investigated the characteristics of the SEP events and their associations with type II and III radio emissions, as well as with their inferred release heights. Moving forward, Section 3 presents the results of the proposed classification/categorization of the SEP events and the outputs of the statistical analysis, and Section 4 concludes this manuscript.

2. Data Selection and Analysis Methods

2.1. Data Selection

For our analysis purposes, we started with the catalog of Paassilta et al. [29], which consists of 176 solar energetic particle (SEP) events that were observed during the years 1997–2016. This list was created based on the SOHO/ERNE proton measurements at 55–80 MeV and on observations of the Electron Proton and Alpha Monitor (EPAM; [30]) on board the Advanced Composition Explorer (ACE; [31]) at 0.18–0.31 MeV for electrons. Based on this catalog of SEP events, we assembled proton and electron data from various sources (to be detailed here below) in order to perform our analysis.

In particular, for the protons, we explored the possibility to extend the study of Paassilta et al. [29] to higher energies. In doing so, the SEPEM (Solar Energetic Particle Environment Modeling)/RDS (Reference Data Set) [32] was used. The SEPEM/RDS delivers 10 differential channels covering energies ranging from 5–200 MeV, which are based on the available measurements of protons from the Geostationary Operational Environmental Satellite (GOES) 5, the GOES 7, the GOES 8, the GOES 11/Space Environment Monitor (SEM), the GOES 13/Energetic Particles Sensor (EPS), and Interplanetary Monitoring Platform 8 (IMP 8)/Goddard Medium Energy (GME). For the electrons, we used data collected by the EPAM instrument onboard the ACE, similarly to [29], at an energy channel of 0.18–0.31 MeV. In addition, we further used seven energy channels of the Wind/3DP instrument of the Wind spacecraft covering an energy range of 0.027–0.520 MeV for the electrons.

The context observation used in this study included the following: solar wind, CMEs, solar flares, and type II and III radio bursts. In particular, the hourly solar wind speed (km/s) data were obtained from the OMNIweb network[1]. In addition, the CMEs were identified from the CDAW CME Catalogue[2] [33], which is based on observations from the Large Angle and Spectrometric Coronagraph (LASCO) on board the SOHO spacecraft [34]. Furthermore, the solar flare intensity, associated with the processes that originated the particles of SEP events, which was recorded in a soft X-rays time series at 0.1–0.8 nm, was obtained from the *Solar Time viewer for AFFects* (STAFF) database[3]. Finally, the presence or absence of type II[4] and type III radio bursts [35,36] was based on the examination of relevant lists and the inspection of radio spectra images by spacecraft (i.e., Wind/WAVES) and ground-based facilities[5]. In particular, decametric–hectometric (DH) type II bursts observed with the Wind/WAVES were utilized in the study. In general, type II bursts occur at all wavelengths (from metric—m—to kilometric—km). Nonetheless, the online catalogue employed in our work provided the range of frequencies of each type II burst. Moreover, type III bursts were identified at a frequency of 14 MHz. In addition, there were cases with multiple type III bursts occurring in high sequences that lasted for a relatively extended time period. These particular cases were identified and used later on as "radio storms".

2.2. Data Analysis and Methods

2.2.1. Onset Time Determination

To automate the determination of the onset time of an SEP event for each energy channel, we developed an algorithm that was applied across all the particle data provided by the GOES/SEPEM for the protons and the ACE/EPAM and Wind/3DP for the electrons. The basic idea of the algorithm aims to create an objective criterion by comparing the detector measurements for a time window where there is no event (counts without fluctuations, i.e., background) with the subsequent measurements. The first step is to determine the average intensity $\overline{J}$ and calculate the standard deviation σ for the given time window; the next step is to compare the subsequent time window measurements with a threshold, defined as $\overline{J} + n \cdot \sigma$, where n is chosen by the user (usually n = 2, 3, or 4). When m consecutive points satisfy this condition (usually m = 3 or 4), then the event onset time in the given channel is defined as the time stamp of the first point above th threshold. If the condition is not fulfilled then the sample window under consideration is moved one point forward in time, then the process is repeated. It is worth mentioning that, in case of pre-event enhancements (such as events that are closely spaced in time or the presence of contamination), the algorithm may fail to determine the onset time (see also [5]).

2.2.2. Velocity Dispersion Analysis

Velocity dispersion analysis (VDA) offers the possibility to calculate the SRTs of the particles emitted from the Sun, as well as the distance traveled from the source to the detector (see details in [29]). VDA assumes that the particles at all energies are released simultaneously and travel the same path length. In particular, the equation of the velocity dispersion in 1 AU shows the aforementioned onset times as a function of the inverse velocity of the particles for the respective energies and is given as follows:

$$T_{onset}(E) = T_{rel} + 8.33 \frac{\text{min}}{\text{AU}} \frac{L(E)}{\beta(E)},$$

where $T_{onset}(E)$ is the observed onset time in min at the particle kinetic energy E, T_{rel} is the release time in min, L is the apparent path length (in AU) traveled by the particles, and $\beta(E)^{-1}$ is the inverse velocity of the particles. According to the VDA assumptions, if energetic particles travel the same path length and are released at the same time, then a linear dispersion relation can be obtained by plotting the particle onset times versus their inverse velocities. As a result, the slope and intersection of the linear fit yields the path length and the particle SRT, respectively. VDA further assumes that the first arriving particles exhibit scatter-free propagation, while their results are subject to the accurate determination of the onset time in the in situ of the particle intensity time profiles. In this work, we considered all 176 SEP events reported in [29] and applied VDA to the

GOES/SEPEM proton differential channels. Out of all of the176 VDA results, there were 41 events with physically acceptable outcomes, namely, with $1 < L \leq 3$ AU. This criterion was observationally established in the work of Vainio et al. [37], who showed that nearly all of the SEP events with an L within this range had reasonable SRTs that were independent of the path length. Moreover, Vainio et al. [37] concluded that, for any L outside of this range, the SRT should not be trusted. In addition, this observational finding was corroborated with a previous study that used simulated data and showed that VDA can yield meaningful results when L ranges between 1 to $\sim$2 AU [38].

2.2.3. Fraction Velocity Dispersion Analysis

The authors in Tan et al. [39] compared the apparent particle path lengths calculated with and without correction to instrumental measurements and suggested that the non-natural results, (e.g., [40]), could be due to contamination of the low-energy channels by the energy deposition of high-energy particles in them. In particular, some of the incident high-energy electrons and protons could scatter out of the detector and contaminate the low-energy channels, thus resulting in the premature detection of lower-energy particles. That is, as the high-energy particles arrive earlier at the satellite, assuming they do not start much earlier than the low-energy particles, they are likely to deposit a fraction of their energy in the lower-energy channels. This gives the false impression that the intensity of the particles corresponding to the low-energy channel has increased, thus resulting in an earlier estimate of the onset time, T_{onset}, of the event for that channel compared to the actual time that the low-energy particles arrive at the detector. Consequently, this would produce early onsets in lower energies and thus would violate the assumptions of VDA. The authors in Kahler and Ragot [40] examined electrons recorded at the ACE/EPAM (0.04–0.31 MeV; with the event being identified at the two higher-energy channels from 0.103–0.31 MeV) and the Wind/3DP (0.025–0.5 MeV). The authors in Tan et al. [39] used electrons measured by the Wind/3DP (0.027–0.510 MeV) and protons from the Wind/*Energetic Particles: Acceleration, Composition, and Transport* (EPACT [41]) (1.4–120 MeV). Nonetheless, substantial contamination was mainly suffered by the low-energy electron channels, in contrast to the protons, which did not exhibit similar behavior.

In order to overcome this problem, we used fractional velocity dispersion analysis (FVDA: [42]) on the Wind/3DP measurements of the electrons. We first found the maximum value j_p in the electron intensity profile and then calculated the time t_η in the rising phase of the intensity profile that satisfied the following relation:

$$j(t_\eta) - j_b = \eta(j_p - j_b),$$

where η is the fractional parameter (we considered $\eta = 3/4$), and j_b is the value of the intensity before the event starts (or the background intensity). The background intensity j_b is considered to be the average value of the intensity in a window of 20 to 30 min before or after the event. According to the above relation, we realized that, for $\eta \to 0$, the time t_η calculated corresponds to the onset time of the event (see details in [42]); however, as already mentioned in the same time interval (for small η), the contamination of the channels is stronger. A fact that was examined by Li et al. [43], who studied various time intensity profiles before and after correcting for contamination by higher-energy channels, revealed that this effect shows a decreasing trend from start to peak in the rising phase. This was the reason why we defined that $\eta = 3/4$.

After the calculation of the time t_η, we followed the same procedure as for VDA, except that in the above equation the T_{onset} time was replaced by the time t_η, thus resulting in finding the release time (T_{rel}) of the electrons from the Sun and the distance they traveled to the Earth. For the 41 SEP events noted above, we applied the FVDA method to the Wind/3DP electron measurements. This resulted in 21 events with physically acceptable values of L (apparent path length). The reason we did not apply this analysis to the entire catalogue was because we wanted to examine the events for which we would have a complete picture of the behavior of both of the particle populations.

2.2.4. Time Shifting Analysis

Time shifting analysis (TSA) essentially “shifts” the detection time of the particles on Earth by a time equal to the time it takes for them to travel through the Parker spiral connecting the Sun and Earth, and it is a later limit for the release of the particles, thus denoting the later limit before which the particles may have been released from the Sun [44]. The equation expressing the above reasoning is as follows:

$$T_{onset} = T_{rel} + \frac{s}{v},$$

where s is the length of the Parker spiral between the Sun and the spacecraft (Earth), and v is the speed of the particles. At this point, we noted that the length of the aforementioned path would be calculated using the Parker Spiral Field Line Model and the average solar wind speed measured in situ on the observing spacecraft via the following relation:

$$s = z(1\mathrm{AU}) - z(\mathrm{R_s}),$$

where,

$$z(r) = \frac{a}{2}[\ln(\frac{r}{a} + \sqrt{1+\frac{r^2}{a^2}}) + \frac{r}{a}\sqrt{1+\frac{r^2}{a^2}}]$$

The coefficient a is equal to $a = u_{sw}/\Omega$, where u_{sw} is the speed of the solar wind, and Ω is the period of the Sun’s equatorial rotation ($2\pi\Omega = 24.47d$). The result of the first relation for T_{rel} represents the latest possible start of the solar energetic particles and is a good approximation if the particles "travel" without scattering and with a tilt angle close to zero along the magnetic field lines. This is the kind of behavior that electrons usually exhibit, and, therefore, the present method was used for the ACE/EPAM electron data. It is worth mentioning that TSA is less accurate than FVDA, and, for this reason, it was used only in cases where FVDA failed to calculate a physically acceptable release time (T_{rel}) of the electrons. In particular, in 6/21 events concluded via the FVDA method, while the length traversed by the particles was reasonably correct, their release times were calculated to be later than the corresponding T_{onset} times of the energy channels, which is impossible. Consequently, for these 6 events, we used the corresponding release times T_{rel}, which were obtained via TSA.

In all of the cases under study, 8.33 min have been added to the obtained SRT in order to facilitate direct comparison with the electromagnetic emission onsets.

3. Results

3.1. SEP Associations with Other Observables

Aiming at a complete presentation of all of the existing information and data for the 21 SEP events under study, we implemented integrated images separately for each event (see an example in Figure 1). These images include all of the particle and solar data we extracted from the databases mentioned in the previous section .

These illustrations feature three types of graphs sharing X and Y axes. The X axis depicts time, thus resulting in a vertical alignment of the three diagrams. The Y axis represents intensity, which varied across the diagrams. The top graph displays soft X-ray radiation fluxes for 0.1–0.8 nm wavelengths, alongside the CME’s height–time profile (for the right y axis, this is the black points and their corresponding linear fit). The middle graph exhibits the proton time profiles at different energies via the SEPEM/RDS, while, in the third graph, the electron recordings from the Wind/3DP are presented.

The top panel of Figure 1 contains two Y axes: one on the left hand side showing the SXR flux values [W/m^2] and one on the right hand side with $\mathrm{R_s}$ units. Apart from the red line, which is the flux values per time for the X-rays, representing the intensity of the solar flare, and the black dots with their corresponding linear fit (black line) concerning the CME height–time evolution taken by the CDAW CME catalogue, additional information is imprinted on the legend of the plot. In particular, this includes the following: (a) the radial speed of the CME, which was computed from the slope of the linear fit (verified against the similar speed obtained from the CDAW CME catalog), (b) the release height for the protons ($H_p(T_{p,rel})$, which is presented as a blue dot), and (c) the release height for the electrons ($H_e(T_{e,rel})$; presented as a green dot). Both (b) and (c) were calculated by assuming that the protons and electrons are released during the propagation/expansion of the driving CME. In particular, the CME height–time evolution was back-extrapolated by assuming a linear dependency. The height of the CME at the time that we previously estimated that the particles would be released (i.e., $T_{p,rel}$ and $T_{e,rel}$) was consequently marked. In addition, we plotted the detection times of type II radio emissions (yellow vertical dashed line). Moreover, the detection time of type III radio emissions (pink line) (or the time interval in the case of a radio storm—pink box), are also added on the top panel. The blue and green boxes indicate the errors in the proton and electron SRTs obtained by VDA and FVDA, respectively.

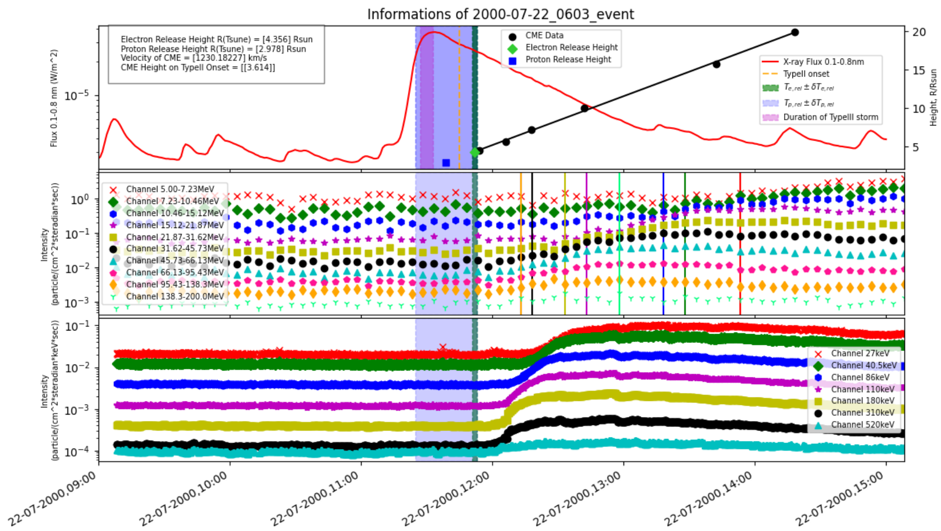

Figure 1. The SEP event on 22 July 2000, 11:30 UTC. The top panel depicts the solar flare in terms of SXRs, together with the CME height–time and the height of release of electrons and protons. The middle panel shows the recordings of the GOES/SEPEM differential proton channels, and the bottom panel demonstrates the electron recordings from Wind/3DP. See text for details.

The middle panel shows the intensity, in units of particle/$(\mathrm{cm}^2 \cdot \mathrm{sr} \cdot \mathrm{MeV} \cdot \mathrm{s})$, versus the time for the ten differential proton energy channels, as obtained from the SEPEM RDS, along with the SEP event onset times T_{onset} (vertical lines) for each energy channel, which were calculated according to the σ method (see Section 2.2.1). Finally, the bottom panel depicts the intensity [particle/$(\mathrm{cm}^2 \cdot \mathrm{sr} \cdot \mathrm{keV} \cdot \mathrm{s})$] time profiles for the seven differential electron energy channels, as obtained from the Wind/3DP.

3.2. The Classification of SEP Events

Based on the release times (T_{rel}) and release time errors (δT_{rel}) of the electrons and protons, we classified the SEP events into three categories: the simultaneous events, the delayed electron events, and the delayed proton events. We should point out here that δT_{rel} was directly obtained by the ordinary least square (OLS) linear fit to the $T_{onset}(b^{-1})$ when applying (F)VDA. In simultaneous events, the release of the protons and electrons is assumed to have occurred concurrently. In this work, simultaneous events are defined as those for which the time sets defined as $(T_{rel,p} - \delta T_{rel,p}, T_{rel,p} + \delta T_{rel,p})$ and $(T_{rel,e} - \delta T_{rel,e}, T_{rel,e} + \delta T_{rel,e})$ have common time points and thus, in essence, overlap. This feature is readily apparent in the integrated images of the events (i.e., it is similar to Figure 1) belonging to this category, with the blue (green) boxes indicating that the aforementioned time intervals appeared to coincide in time.

On the other hand, the delayed proton events were characterized by an earlier release of the e^- than the p^+. In such a case, the blue frame depicting the timing of the protons is located after the corresponding green frame of the electrons. Similarly, the delayed electron events are characterized by an earlier release of the protons. In this case, the green frame (i.e., for the electrons) follows the blue one (i.e., for the protons).

It is worth mentioning that, out of the total 21 SEP events, the simultaneous events were 13/21 (62%), the delayed protons events were 5/21 (24%), and the delayed electrons events were 3/21 (14%).

3.3. Analysis

3.3.1. Path Lengths for Protons and Electrons: $L_p(L_e)$

Figure 2 compares the derived path lengths for the protons and electrons for the 21 events that have been analyzed. The protons seem to be characterized by lengths L_p ranging from 1–3 AU, i.e., within the whole physically acceptable range that we have defined from the beginning; on the other hand, the electrons seem to take values L_e from 1–1.75 AU. Thus, the SEP events were divided into two basic categories. The first category concerns events for which L_p = 1–2 AU and L_e = 1–1.75 AU (14 out of 21, 66.66%), while the second category is characterized by L_p = 2–3 AU and L_e = 1–1.75 AU (7 out of 21, 33.33%). Krucker and Lin [20] made a similar separation, except that they did not have such a large variance in the $L_p(L_e)$ diagram; thus, for the first category it was L_p = 1.1–1.5 AU and L_e = 1–1.5 AU, and for the second category it was L_p = 1.7–2.2 AU and L_e = 1.1–1.3 AU. It is worth noting that in [20], 18 out of 26 events, i.e., 70%, belonged to the first category, while the remaining 8 events, i.e., 30%, were part of the second category, which is consistent with our results.

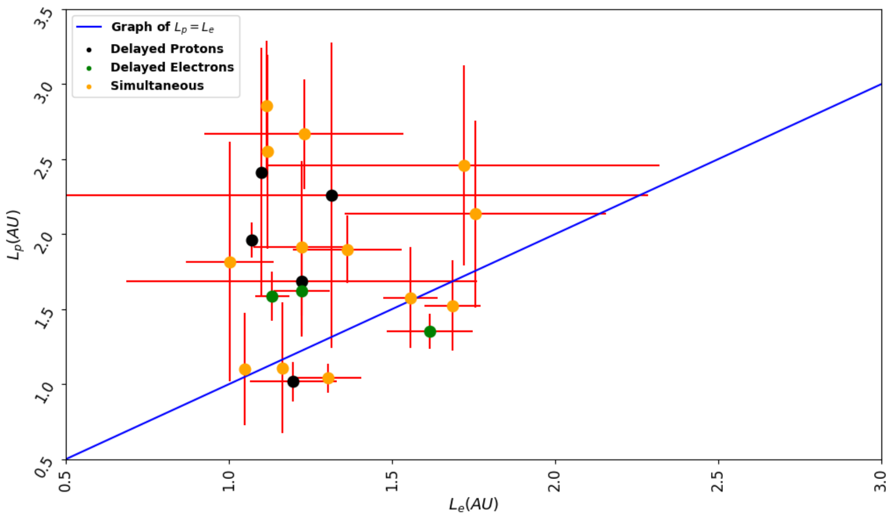

Figure 2. Chart $L_p(L_e)$. Black points correspond to delayed proton events, green points to delayed electron events, and yellow points to simultaneous events. The red bars indicate the errors of L_p and L_e.

3.3.2. Proton Event Groups

Figure 3 provides the length that the protons traveled (L_p) as a function of the difference between the release time of the protons and electrons ($Dt_{rel} = T_{p,rel} - T_{e,rel}$). As can be seen, simultaneous events (denoted as yellow stars) spanned over L_p = 1–3 AU. Moreover, all of the 13 simultaneous events fell between Dt_{rel} = [−20 min, 50 min], while 11/13 had a Dt_{rel} = [−20 min, 15 min]. Since we are focusing on simultaneous events, the Dt_{rel} should not be large. As for the delayed proton events (denoted as black dots), we observed a larger spread on the Dt_{rel}, which spanned from [15 min, 130 min], with L_p spans between 1 and 2.5 AU. On the other hand, the delayed electron events (denoted as green dots) were localized in a very specific region from [−10 min, −5 min] and from 1.35 AU to

1.65 AU. Based on Figure 3, we separated the events into two main groups. The first group (Group 1) contains 14 events (66.66%) with L_p values varying between 1 and 2 AU and a Dt_{rel} varying from [−25 min, 78 min], while the second group (Group 2) contains 7 events (33.33%) with L_p values varying between 2 and 2.7 AU and a Dt_{rel} varying from [−13 min, 125 min]. For comparison, Krucker and Lin's [20] first group contained 18 events (70%) with L_p values varying between 1 and 1.5 AU and a Dt_{rel} varying from [20 min, 200 min], while the second group contained 8 events (30%) with L_p values varying between 1.6 and 2.2 AU and a Dt_{rel} from [−25 min, 40 min].

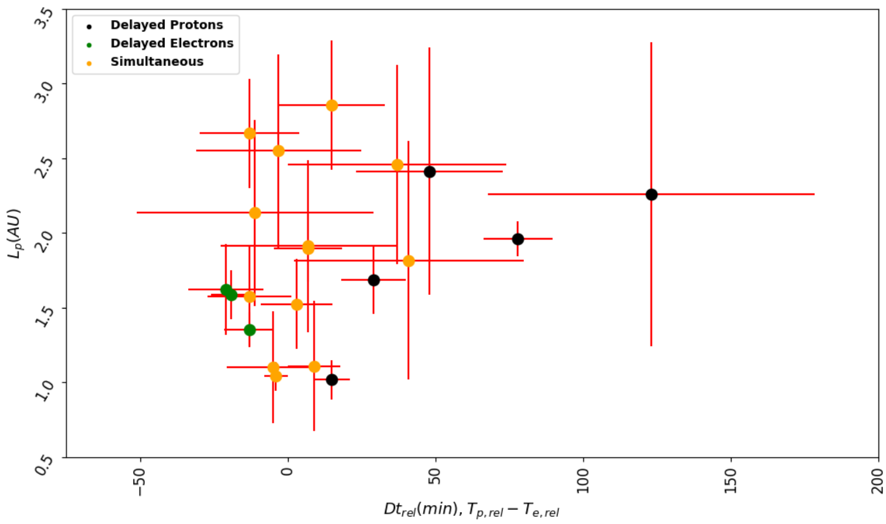

Figure 3. $L_p(Dt_{rel})$. Black points correspond to delayed proton events, green points to delayed electron events, and yellow points to simultaneous events. The red bars indicate the errors of L_p and Dt_{rel}.

3.3.3. Proton Events, Temporarily Related Electron Events, and Release Episodes

Figure 4 provides the Dt_{rel} as a function of the time difference between the proton release time and the onset time of type III radio emissions at 14 MHz ($T_{p,rel} - T_{typeIII}$). Simultaneous events were concentrated in a range from [0 min,50 min], while, when focusing on the 11/13 events, this interval shifted to [0 min, 25 min]. Similarly, the Dt_{rel} for the simultaneous events fell within [−15 min, 40 min] and was narrowed to [−15 min, 15 min] for the 11/13 sample. Therefore, the release of protons is temporally related to the release of electrons and to the onset of type III radio bursts. On the other hand, the delayed p^+ events seemed to take large positive values on both axes, while the delayed e^- events were characterized by a very small range of values with the time differences Dt_{rel} and $(T_{p,rel} - T_{typeIII})$, which ranged from [−20 min, −10 min] and from [−10 min, −5 min], respectively. Moreover, for the set of 21 events of this study, a linear relationship between the Dt_{rel} and $T_{p,rel} - T_{typeIII}$ was clear, thus indicating that the longer the injection of the protons into space was delayed with respect to the observation of type III radio emissions, the longer it was delayed with respect to the release of the electrons. This behavior, and by extension the line describing it, appears to be common to both types of events. The same observation was underlined by Ameri et al. [28], who implemented a similar representation (their Figure 5b) for a statistical sample of 45 SEP events. They also pointed out the fact that simultaneous events seem to be concentrated in small differences between Dt_{rel} and $T_{p,rel} - T_{typeIII}$, while delayed events are characterized by larger time differences, which is a point that we also made based on our diagram.

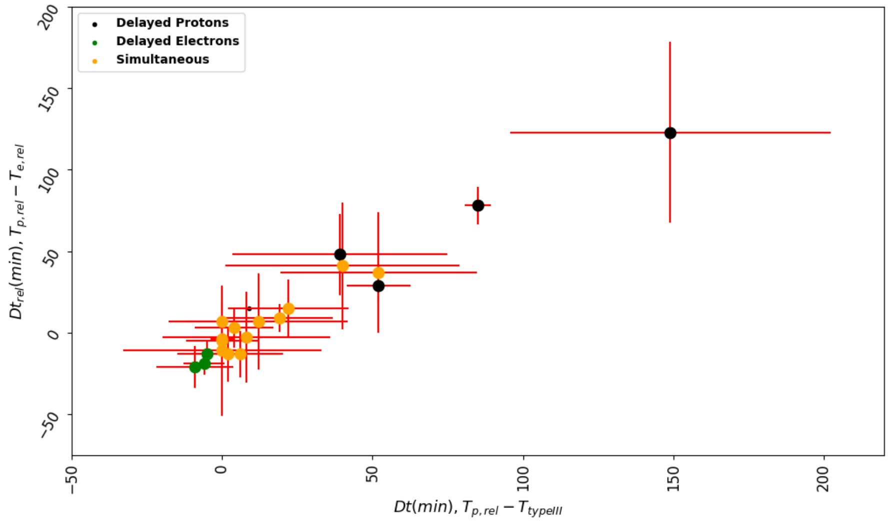

Figure 4. $Dt_{rel}(T_{p,rel} - T_{typeIII})$. Black points correspond to delayed proton events, green points to delayed electron events, and yellow points to simultaneous events. The red bars indicate the errors of Dt_{rel} and $T_{p,rel} - T_{typeIII}$.

Figure 5 presents the relation between the Dt_{rel} and the time difference between the release of the protons and the observation time of the DH type II radio burst ($Dt = T_{p,rel} - T_{typeII}$). Figure 5 seems similar to Figure 4, yet it contains the 16/21 SEP events we have focused on, because, for the remaining five events, no type II radio emission was identified. For the simultaneous events, the Dt ranged from [−35 min, 50 min], while the Dt_{rel} ranged from [−15 min, 40 min] when noticing that, for 8/10 of the simultaneous events (i.e., yellow points), the variance decreased to [−15 min, 15 min]. This characteristic becomes apparent if we omit the two (highest) yellow points reflecting simultaneous events, which were characterized by $Dt_{rel} \approx 50$ min. For the four delayed Dt_{rel} events, there was a large range of values on the positive semiaxes X and Y, from [20 min,150 min] and from [15 min, 125 min], respectively. On the other hand, the two delayed e^- events occurred at approximately the same points, with a Dt_{rel} = −20 min and a $(T_{p,rel} - T_{typeII})$ =−35 min. In addition to the nearly equal time differences for the plots, $Dt_{rel}(T_{p,rel} - T_{typeIII})$ and $Dt_{rel}(T_{p,rel} - T_{typeII})$, an additional common feature is their linearity. For the set of 16 SEP events, we saw that, as the Dt_{rel} increased, the $T_{p,rel} - T_{typeII}$ also increased. This indicates that the longer the proton release is delayed with respect to the type II radio emissions, the longer it is delayed with respect to the release of the electrons. Thus, the general trend visible in Figures 4 and 5 is that the difference between the proton and electron release times (Y axis in both of the Figures) increases with the increasing difference between the proton release time and the type III onset time (Figure 4) or the type II onset time (Figure 5). As a result, for the simultaneous events, the protons seem to be released in temporally more close relation to the electrons (Y axis in both of the Figures) escaping into the IP medium, which most possibly follow magnetic reconnection processes producing the electron beams leading to radio type III emission.

Figure 6 depicts the difference between the proton release times and type III onset ($T_{p,rel} - T_{typeIII}$) and the electron release times and the type III onset ($T_{e,rel} - T_{typeIII}$) for all of the 21 SEP events. As can be seen, all of the SEP events were concentrated on the positive X axis part, with the time difference $T_{e,rel} - T_{typeIII}$ ranging—for simultaneous events—from [0 min, 20 min] and for the delayed proton and electron events from [0 min, 25 min] and [0 min, 10 min], respectively. Therefore, it seems that the release of electrons occurs at the same time or shortly after the emission of the type III radio burst. In contrast, the Y axis revealed a wide range of values, from [10 min, 150 min] for the delayed proton events, while, for the delayed electron events, this range fell within [−10 min,−5 min]. In addition, the 13 simultaneous events took values between [0 min, 50 min], with 11 of them ranging from [0 min, 20 min]. As a result, the majority of the simultaneous events were characterized by proton releases in close proximity to type III radio bursts. On the other hand, the delayed proton events had a wide range of values, and the protons predominantly appeared to be released after the type III onset. For the delayed electron events, the protons were released earlier but were still close to the type III radio emissions, while the electrons were injected into IP space later, but still within 10 min after the aforementioned radio bursts. It should be noted that, in [28], the same diagram with inverted axes, i.e., $T_{e,rel} - T_{typeIII}(T_{p,rel} - T_{typeIII})$, found a linear correlation for each type of event, simultaneous and delayed, which does not appear in our results.

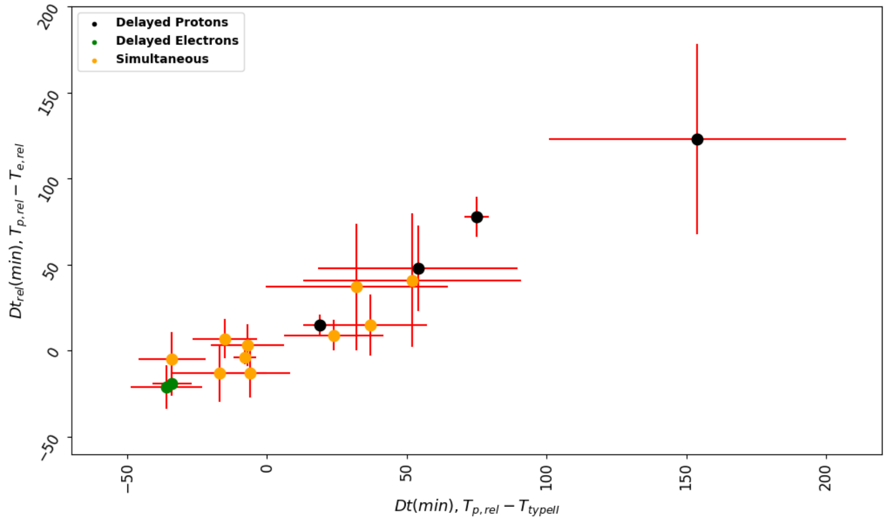

Figure 5. $Dt_{rel}(T_{p,rel} - T_{typeII})$. Black points correspond to delayed proton events, green points to delayed electron events, and yellow points to simultaneous events. The red bars indicate the errors of Dt_{rel} and $T_{p,rel} - T_{typeII}$. The included events are 15/21; as for the remaining 6, it was not possible to identify the region where the respective solar flare occurred.

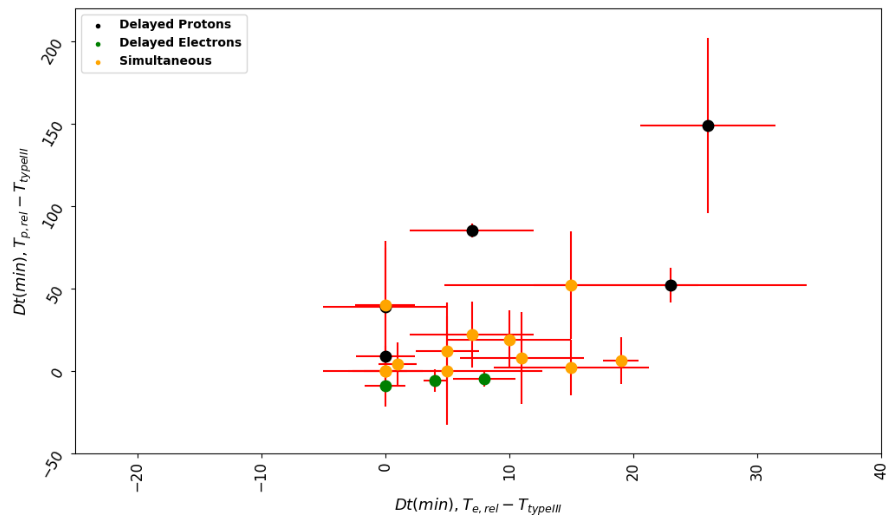

Figure 6. $T_{p,rel} - T_{typeIII}(T_{e,rel} - T_{typeIII})$. Black points correspond to delayed proton events, green points to delayed electron events, and yellow points to simultaneous events. The red bars indicate the errors of $T_{p,rel} - T_{typeIII}$ and $T_{e,rel} - T_{typeIII}$.

Figure 7 is similar to Figure 6 but with respect to the type II onset time (i.e., $T_{p,rel} - T_{typeII}(T_{e,rel} - T_{typeII})$) for the 16 SEP events with identified type II bursts. For the four black dots (delayed protons), a relatively small spread was observed on the X axis, with values ranging from −5 min to 30 min, and a significantly larger range was observed on the Y axis, with values ranging from 2 min to 150 min. The two green dots (delayed electrons) were located almost at the same points, with $T_{p,rel} - T_{typeII} = -35$ min and $T_{e,rel} - T_{typeII} = -15$ min. The statistical sample for the set of delayed events was quite small, only six events, yet they seemed to show a linear dependence between them. For the delayed proton events, we observed a similar behavior to that of the $T_{p,rel} - T_{typeIII}(T_{e,rel} - T_{typeIII})$ diagram, i.e., the release of p^+ particles into IP space well after the type II radio bursts (>30 min) and the release of e^- particles relatively close to the radio emissions.

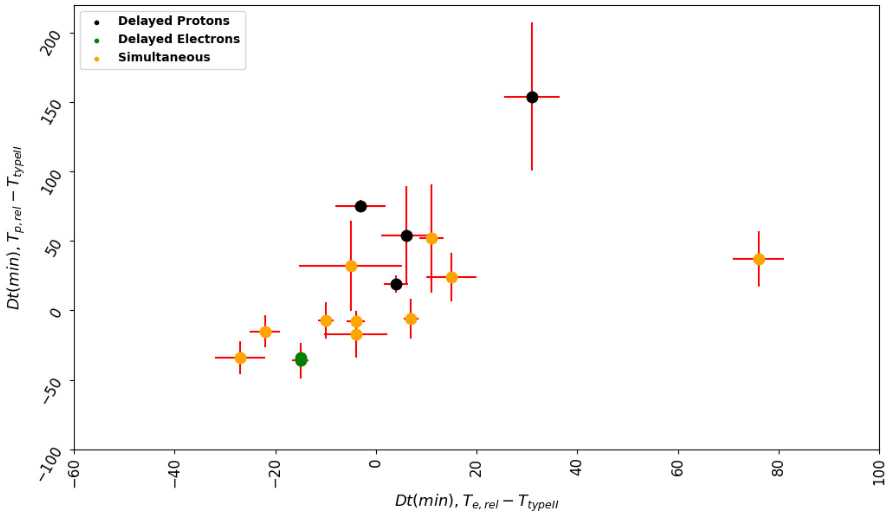

Figure 7. $T_{p,rel} - T_{typeII}(T_{e,rel} - T_{typeII})$. Black points correspond to delayed proton events, green points to delayed electron events, and yellow points to simultaneous events. The red bars indicate the errors of $T_{p,rel} - T_{typeII}$ and $T_{e,rel} - T_{typeII}$. The included events are 15/21; as for the remaining 6, it was not possible to identify the region where the respective solar flare occurred.

For the simultaneous events, a linearity indicates that when the time difference $T_{p,rel} - T_{typeII}$ increases, the time difference $T_{e,rel} - T_{typeII}$ also increases. For these events, the range of values for the X and Y axes is from −20 min to 75 min and from −35 min to 50 min, respectively. In addition, we observed a group of six simultaneous events where they were characterized by negative $T_{p,rel} - T_{typeII}$ and $T_{e,rel} - T_{typeII}$ values; therefore it was not improbable to suggest that particles were released prior to the detection of the DH type II radio emissions. Thus, one may assume that the dominant contributor in these events was the solar flare and not the CME. At the same time, it could be the case that the shock was still evolving (from 2–4 R_{SUN}), and it was either not yet supercritical, or the geometry of the shock was not oblique to the quasiperpendicular, both of which are necessary conditions for the radio type II emission to be produced by a CME-driven shock [45].

3.3.4. Release Episodes and the Location of the Solar Source

Figure 8 presents the difference between the proton start times and the onset of the type III radio bursts as a function of the event connection angle ($\Delta\Phi$). This refers to the longitudinal distance and was calculated as follows:

$$\Delta\Phi = \phi_{fl} - \frac{\Omega_{\odot}^{-1} r_{s/c}}{u_{sw}} \quad (1)$$

where ϕ_{fl} is the solar flare longitude, $2\pi\Omega_{\odot}^{-1}$ = 24.47d is the equatorial period of the solar rotation, $r_{s/c}$ is the radial distance of the spacecraft from the Sun, and u_{sw} is the average solar wind speed at the time of the SEP event observed onset. The longitudinal distance of the footpoint from the flare location is positive if the flare is to the west from the footpoint and negative if the flare is to the east. The total number of events considered in the present case was 15, 6 delayed and 9 simultaneous, because, for the remaining 6 events, it was not possible to detect the respective flare and thus calculate its connection angle due to the fact that the event originated behind the solar limb.

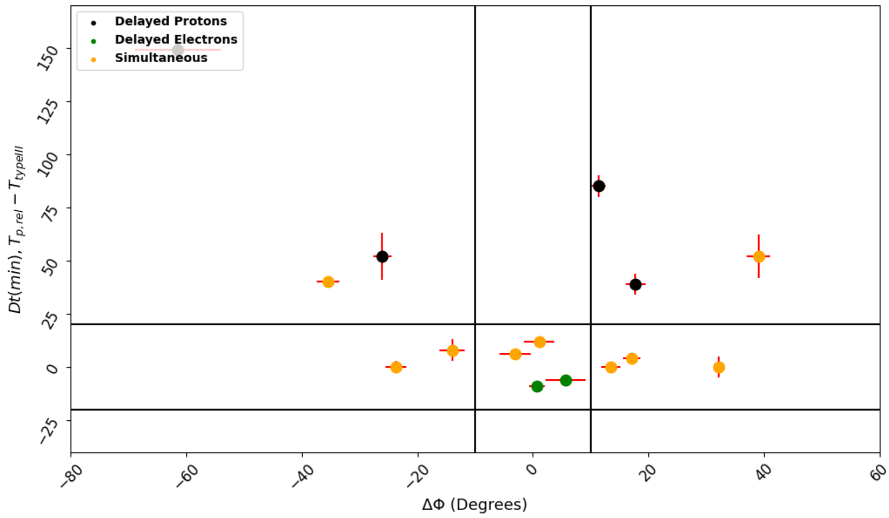

Figure 8. $T_{p,rel} - T_{typeIII}(\Delta\Phi)$. Black points correspond to delayed proton events, green points to delayed electron events, and yellow points to simultaneous events. The black solid lines represent $T_{p,rel} - T_{typeIII}$ = +/ or −20 min and ΔΦ = +/− 10^o forming a region characterized by good magnetic connection and proton release times close to the onset of type III radio emissions. See text for details.

The vertical lines in Figure 8 indicate a range from $-10°$ to $10°$ for the X axis and the horizontal lines indicate a range from -20 min to 20 min for the Y axis. Based on the diagram, simultaneous events had a ΔΦ from $-40°$ to $40°$ and a $T_{p,rel} - T_{typeIII}$ from -10 min to 50 min. The delayed p^+ events had a ΔΦ from $-60°$ to $20°$ and a $T_{p,rel} - T_{typeIII}$ from 40 min to 150 min, while the delayed electron events presented a ΔΦ from 0 to $5°$ and a $T_{p,rel} - T_{typeIII}$ from -10 min to -5 min. Therein, the simultaneous events seemed to be concentrated at relatively small time differences of $T_{p,rel} - T_{typeIII}$ and small connection angles of ΔΦ, with 8 out of 10 being located between -20 min and 20 min and being located between $-25°$ and $35°$; similarly, the delayed e^- events were characterized by very small connection angles and time differences. In contrast, the delayed proton events exhibited large dispersions on both axes and were identified as we move away from $\Delta\Phi = 0^o$. The authors in [28] presented a similar Figure (their Figure 6a) for the set of the 41 events they studied, without separating them into simultaneous and delayed. However, both illustrations (Figure 8 of the current work and Figure 6a in their article) have similarities in terms of the events' distributions along the axes.

Figure 9 is similar to Figure 8 but demonstrates the electrons' release. In this particular case, the simultaneous events had a ΔΦ ranging from -40^o to 40^o, which is to be expected, since we are considering the same SEP events, and they had a time difference, $T_{e,rel} - T_{typeIII}$, that ranged from 0 min to 20 min. Similarly, the delayed p^+ events were characterized by a ΔΦ ranging from -60^o to 20^o and by a $T_{e,rel} - T_{typeIII}$ ranging from 0 min to 25 min, while the delayed e^- events were identified very close to zero on both axes. The simultaneous and delayed e^- events were concentrated at relatively narrow ΔΦ values, and the delayed p^+ events showed a larger dispersion. Ameri et al. [28] were able to associate electron events with the initially considered proton events for 22/41 events, which are presented in their Figure 6b, which is similar to Figure 9. Upon comparing these two, a similar behavior with respect to the dispersion of the events along the axes is apparent. Upon focusing on each group, it can be observed that the delayed p^+ events appeared to cluster around very negative values of ΔΦ and larger time differences, (i.e., $T_{e,rel} - T_{typeIII}$) when compared to the simultaneous events in each Figure. Generally, simultaneous events are characterized by a ΔΦ around 0^o and by a small $T_{e,rel} - T_{typeIII}$, thus indicating that the electrons were released together with or shortly after the type III burst.

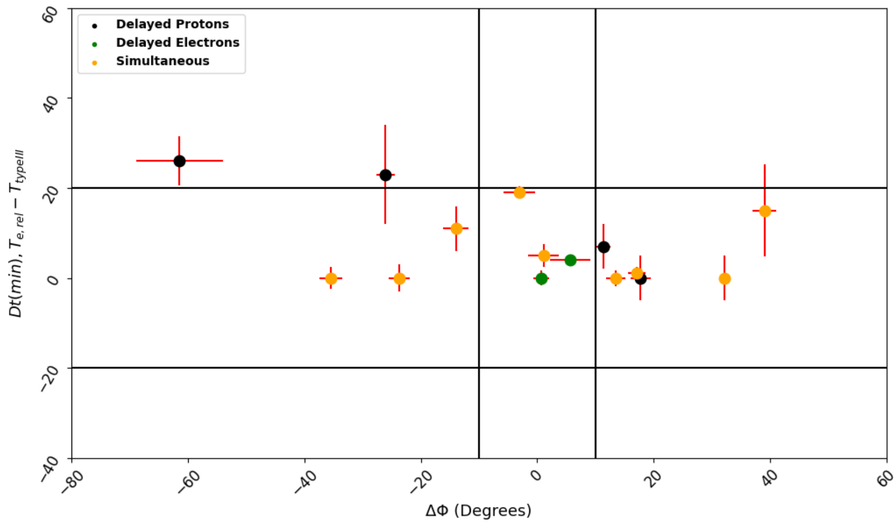

Figure 9. $T_{e,rel} - T_{typeIII}(\Delta\Phi)$. Black points correspond to delayed proton events, green points to delayed electron events, and yellow points to simultaneous events. The black solid lines represent $T_{e,rel} - T_{typeIII} = -20$ min, $T_{e,rel} - T_{typeIII} = 20$ min, $\Delta\Phi = -10^o$, and $\Delta\Phi = 10^o$, thereby creating a region characterized by good magnetic connection and electron release close to type III radio emissions.

Figure 10 is similar to Figure 8 but for type II bursts. Figure 10 and the following Figure 11 that presents the relation ($T_{e,rel} - T_{typeII}(\Delta\Phi)$) include 12/21 events, of which 5/12 were delayed and 7/12 were simultaneous. The reason we omitted the remaining 9 out of the total 21 events is that it was not possible to detect both the respective solar flares and/or the type II radio burst. As for the simultaneous events, the values of the time difference $T_{p,rel} - T_{typeII}$ ranged from -35 min to 50 min, and the $\Delta\Phi$ values ranged from -40^o to 40^o, respectively; for the delayed p^+ events, the values of the Y axis were from 50 min to 155 min, and the values of the X axis were from -60^o to 20^o. In addition, the delayed e^- events were close to a $\Delta\Phi = 0^o$ and a $T_{p,rel} - T_{typeII} = 0$ min, thus confirming that they were located in specific regions, which did not suffer as large time differences as the delayed p^+ events. The smaller the $\Delta\Phi$ of an event, the more the protons are released closer to the onset of the type II radio bursts, i.e., the smaller the time difference $T_{p,rel} - T_{typeII}$ is. In general, simultaneous events demonstrate a small dispersion along both axes and seem to be concentrated in regions characterized by a small $\Delta\Phi$ and $T_{p,rel} - T_{typeIII}$. In contrast, the late p^+ events, although few in number, tended to have the same behavior as that of Figures 8 and 9, which were characterized by large dispersion.

The finding that the time difference $T_{p,rel} - T_{typeII}$ increased when $\Delta\Phi$ became larger can be explained if one considers that type II radio bursts are related to the propagation of a CME-driven shock wave. In order to observe an SEP event in situ, a magnetic connection should be established between the source at the Sun and the observer (i.e., at Earth). Therefore, when an SEP event takes place at a large $|\Delta\Phi|$ (as in an absolute value) the resulting particle flux cannot be immediately detected. Hence, time is needed before the CME-driven shock wave propagates outwards [46,47], thus intersecting the magnetic field lines to establish a magnetic connection. As a result, this may explain why the difference between the particles' release times and the detection times of the type II radio bursts increases as $\Delta\Phi$ becomes larger.

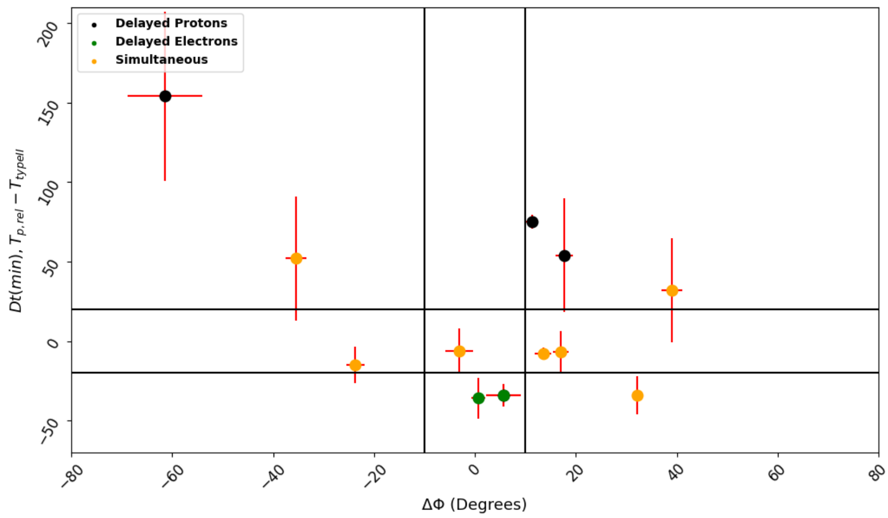

Figure 10. $T_{p,rel} - T_{typeII}(\Delta\Phi)$. Black points correspond to delayed proton events, green points to delayed electron events, and yellow points to simultaneous events. The black solid lines represent $T_{p,rel} - T_{typeII} = -20$ min, $T_{p,rel} - T_{typeII} = 20$ min, $\Delta\Phi = -10^o$, and $\Delta\Phi = 10^o$, thus creating a region characterized by good magnetic connection and proton release near type II radio emissions.

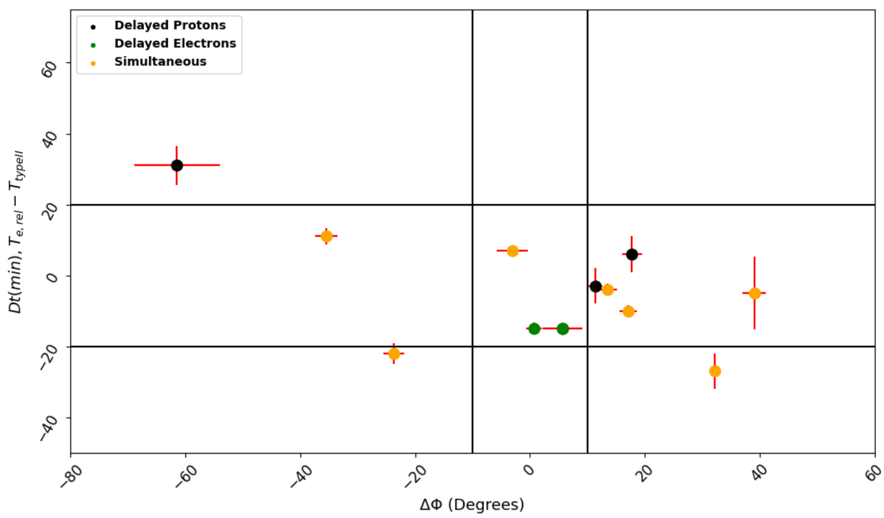

Figure 11. $T_{e,rel} - T_{typeII}(\Delta\Phi)$. Black points correspond to delayed proton events, green points to delayed electron events, and yellow points to simultaneous events. The 4 black lines represent the lines $T_{e,rel} - T_{typeII} = -20$ min, $T_{e,rel} - T_{typeII} = 20$ min, $\Delta\Phi = -10^o$, and $\Delta\Phi = 10^o$, thus creating a region characterized by good magnetic connection and electron release near type II radio emissions.

Figure 11 examines the relationship between the time difference between the electron release times and the onset times of type II radio bursts as a function of $\Delta\Phi$ for the 12/21 events mentioned above. The features observed were similar to those of Figure 10 except for the variance on the Y axis, $T_{e,rel} - T_{typeII}$, which was much smaller for the set of events and for each group separately. More specifically, the simultaneous events had a $\Delta\Phi$ from -40^o to 40^o and a $T_{e,rel} - T_{typeII}$ from -25 min to 10 min, while the connection angle of the delayed p^+ events ranged from -60^o to 20^o, and the time difference $T_{e,rel} - T_{typeII}$ ranged from -5 min to 30 min. Correspondingly, the delayed e^- events had characteristic connection angles from 0^o to 5^o and a time difference of $T_{e,rel} - T_{typeII} = -15$ min. The time difference $T_{e,rel} - T_{typeII}$ grows as the absolute value of the connection angle $\Delta\Phi$ increases, which may possibly be attributed to a shock wave propagation and its relation to the magnetic connection of the observer, as shown in Figure 10.

3.3.5. Release Episodes and Shock Heights

The relation between the height of the proton injection ($H_{p,rel}$) into space and the heliographic longitude of the solar flare (ϕ_{sf}) is presented in Figure 12. At this point, it should be noted that 12 of the total 21 events were included in this diagram, because, for the rest, it was impossible to determine either the location of the associated solar flare or the detection time of the type II radio bursts. Plotted in blue, green, and orange are $H_{p,rel}$ for the delayed p^+ events, for the delayed e^- events, and for the simultaneous events, respectively, and in black are the CME heights at the time of detection of the type II radio bursts (H_{typeII}). In addition, the parabolic relation optimally describing the height $H_{p,rel}$ as a function of the heliographic longitude of the flare ϕ_{sf} is included in magenta color. The coefficients of this parabolic relation are imprinted on the legend. This parabolic fit was compared with the one presented in [48] and added with a gray parabola. It is worth mentioning that the events in our study were moderately (ϕ_{sf} = [15°, 45° & 75°, 90°]) or well connected (ϕ_{sf} = [45°, 75°]), while [48] presents a fit covering ϕ_{sf} = [−20°, 120°] (their Figure 4).

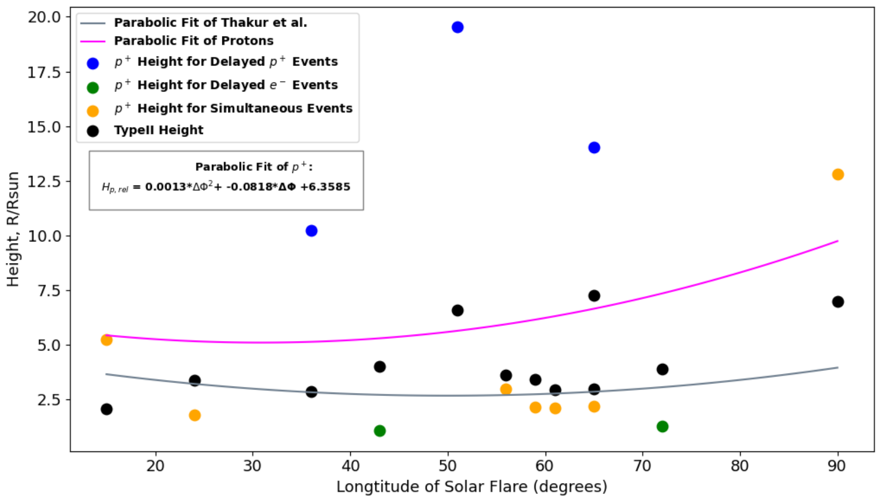

Figure 12. Illustration of the diagram $H_{p,rel}(\phi_{sf})$, in which is included the height of the CME at the time of observation of type II radio emissions and the graph, $H_p = 0.0013\phi_{sf}^2 - 0.0818\phi_{sf} + 6.3585$, describing the relationship between the proton release height and the heliographic longitude of the flare. In addition, for comparison purposes, the parabola calculated in paper [48] is also included.

As can be seen, in 8/12 events the protons started from heights below 5R$_s$, while the remaining 4 were characterized by $H_{p,rel} > 10R_s$. At the same time, at heliographic longitudes from 45° to 75°, i.e., well-connected events, it appears that the proton release occurred close to but prior to the detection of type II radio emissions, since the CME height at the time of observation of these radio bursts exceeded the height of the particle injections into space. Therefore, in the region of well-connected events, 6/8 events had an earlier proton release than the detection of DH type II radio emissions. This can be explained as follows: (a) solar flares may have played a more important role in the acceleration and release of protons compared to the CME shock wave; (b) the onset time of the DH type II burst used in this work may have been delayed with respect to the release of the protons; and (c) transport effects low in the corona, e.g., adiabatic cooling, with perpendicular diffusion/transport may have had an important role in the obtained release time of the particles. The remaining 2/8 events in this region were delayed proton events with $H_{p,rel} \gg H_{typeII}$, thus indicating that shock waves were established and contributed to the acceleration and injection of protons into IP space. As we move away from the region characterizing the well-connected events, a larger dispersion in the values of $H_{p,rel}$ could be observed, which is most likely related to the CME propagation and the moderate connectivity of these events. That is, the worse the connection is of an event, the more time, and hence height, it takes for the CME to establish magnetic connection. Thus, while the particles may have been released earlier, we were not able to calculate the actual time of their injection into IP space, because the flux of p^+ and e^- that we measure and through which we find $T_{p,rel}$ and $T_{e,rel}$ (see VDA and FVDA) rises once they travel along the appropriate magnetic field lines to get to our detector. In contrast, in an event occurring in a region of the Sun where its surface is directly magnetically connected to the Earth, the particles will be detected without further delay such that the calculation of $T_{p,rel}$ and $T_{e,rel}$ is consistent with their actual injection time into space. The crucial role played by the CME on the particle observation time prompted Thakur et al. [48] and ourselves to establish the aforementioned parabolic relation. Upon comparing our results with those of [48], we observe that the two relations are very close to each other, and if full coverage of the ϕ_{sf} was possible in our sample, a better match would possibly have been obtained. More specifically, in that paper they calculated that $H_{p,rel} = 0.0008\phi_{sf}^2 - 0.08\phi_{sf} + 4.67$, while we calculated that $H_{p,rel} = 0.0013\phi_{sf}^2 - 0.0818\phi_{sf} + 6.3585$ (Figure 12). We also calculated the errors of the coefficients of this equation and concluded that $\alpha = 0.00133 \pm 0.00398$, $\beta = -0.08178 \pm 0.41332$, and $\gamma = 6.35851 \pm 10.16603$, where α is the coefficient of ϕ_{sf}^2, β is the coefficient of ϕ_{sf}, and γ is the constant. ($H_p = \alpha \cdot \phi_{sf}^2 + \beta \cdot \phi_{sf} + \gamma$).

Figure 13 is similar to Figure 12 but for electrons. Since, in [48], electron events were not considered, our generated parabola for the electrons will be compared to those for the protons.

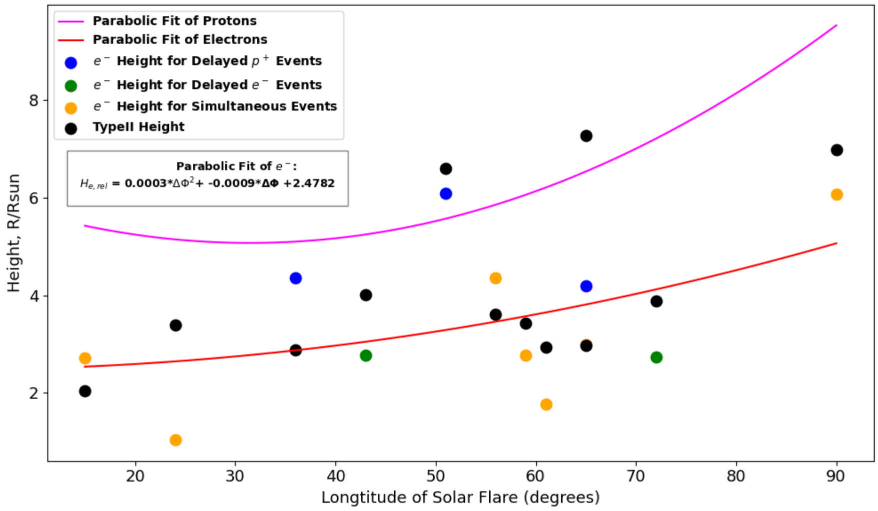

Figure 13. $H_{e,rel}(\phi_{sf})$ illustration of the height of the CME at the time of observation of type II radio emissions and the graph, $H_e = 0.0003\phi_{sf}^2 - 0.0009\phi_{sf} + 2.4782$, describing the correlation between the electron release height and the heliographic longitude of the flares. Note that there are two events with $\phi_{sf} \simeq 65^o$ and $H_e \simeq 4\mathrm{R_s}$ that appear as one blue point but have different H_{typeII}. The corresponding graph of protons (H_p) is also included for comparison.

The lower starting heights of the electrons compared to those of the protons, [6] and the smaller time differences $T_{p,rel} - T_{typeII}$ compared to $T_{e,rel} - T_{typeII}$ (see Figure 7), is expected given that the parabola, ($H_e = \alpha \cdot \phi_{sf}^2 + \beta \cdot \phi_{sf} + \gamma$), will be characterized by a smaller constant γ. Moreover, it is reasonably derived that the α coefficient of ϕ_{sf}^2 is smaller, which implies that the generated parabola will be wider than its p^+ counterpart behavior. Thus, upon observing Figure 13, the obtained parabola is valid, as everything we have mentioned applies to the secondary equation we calculated, $H_{e_rel} = 0.0003\phi_{sf}^2 - 0.0009\phi_{sf} + 2.4782$, while at the same time it does not differ much from the corresponding two p^+ relations mentioned above. The errors of the coefficients of the above equation are $\alpha = 0.00033 \pm 0.00091, \beta = -0.00089 \pm 0.09431$, and $\gamma = 2.47823 \pm 2.31978$, where $H_e = \alpha \cdot \phi_{sf}^2 + \beta \cdot \phi_{sf} + \gamma$.

Regarding the relationship between $H_{e,rel}$ and H_{typeII}, we found, as before, that in the regions characterizing the well-connected events with heliographic longitude from 45° to 75°, the electrons were injected into space at heights close to the values of the corresponding H_{typeII}, while, as we move away from this range, the dispersion exhibited by $H_{e,rel}$ increased. Similar to what we discussed in Section 3.3.5 for protons, the 6/8 well-connected events had electron releases earlier than the observation of type II radio emissions, thus eventually indicating the importance of solar flares in the acceleration and injection into IP space for both electrons and protons. At the same time, the remaining two well-connected delayed proton events, the same ones reported in Figrue 12, also had $H_{e,rel} > H_{typeII}$, thus concluding that in these cases both particle populations were accelerated and released mainly during the CME propagation. Continuing the commentary for all the heliographic longitudes, the values obtained for the electron release height were less than $5R_s$ for 10 of them and greater than $6R_s$ for the remaining 2, which were, however, also characterized by correspondingly large H_{typeII} values. We further distinguish that, in four cases, $H_{e,rel} > H_{typeII}$ held, which we also pointed out in five proton events ($H_{p,rel} > H_{typeII}$). The fact that the particles were released later than in type II radio bursts suggests that, in these cases, the CME probably played a more crucial role compared to the solar flare in question. In conclusion, of the aforementioned four and five electron and proton events, respectively, three of them were those associated with the same SEP events, with the result that these events were entirely characterized by particles released at higher altitudes than the CME height at the time of observation of the type II radio emissions.

The injection heights of the protons and electrons in space ($H_{p,rel}$ and $H_{e,rel}$), as well as the height of the CME of each event at the time of detection of the type II radio bursts (H_{typeII}), are summarized in Figure 14. The top histogram counts electrons and protons together, while the bottom contains the values of the heights associated with the aforementioned radio emissions. In addition, the mean, median, and standard deviation for each set are reported in Table 1. We first note that the protons could be injected into space at quite high heights, higher than $10R_s$, while in the case of the electrons, all of the events had $H_{e,rel} < 5R_s$, except for two that received a value of H_e slightly above $6R_s$. Furthermore, the electrons were characterized by a small mean ($mean = 3.48R_s$) and standard deviation ($std = 1.33R_s$), so we realized that they had a tendency to be injected into the IP medium when still close to the Sun. This is in contrast to the protons, where they generally showed that they were injected into space at a higher $H_{p,rel}$, with a $mean = 5.27R_s$, and their release height showed a larger dispersion, since $std = 4.87R_s$. Nevertheless, according to the histogram, most events took values of $H_{p,rel}$ and $H_{e,rel}$ that ranged from $1R_s$ to $5R_s$. Regarding the heights of the CME at the moment of detection of the type II radio emissions, we observe the same behavior and values as those of the electrons, i.e., low values for the mean ($mean = 3.89R_s$) and standard deviation ($std = 1.71R_s$) of this sample.

Table 1. The CME heights at the time of the release of e^- and p^+ events and at the onset of the DH type II radio emission.

	Mean (R/R_s)	**Median (R/R_s)**	**Standard Deviation (R/R_s)**
e^-	3.48	3.13	1.33
p^+	5.27	3.44	4.87
$TypeII$	3.89	3.41	1.71

By extension, the type II radio bursts appeared to be emitted, while the CME's shock wave was at a low altitude, without deviating much from this behavior. In particular, for the set of events, only three times did the H_{typeII} height exceed $5R_s$, where in these cases the heights were $6.6R_s$, $6.98R_s$, and $7.26R_s$.

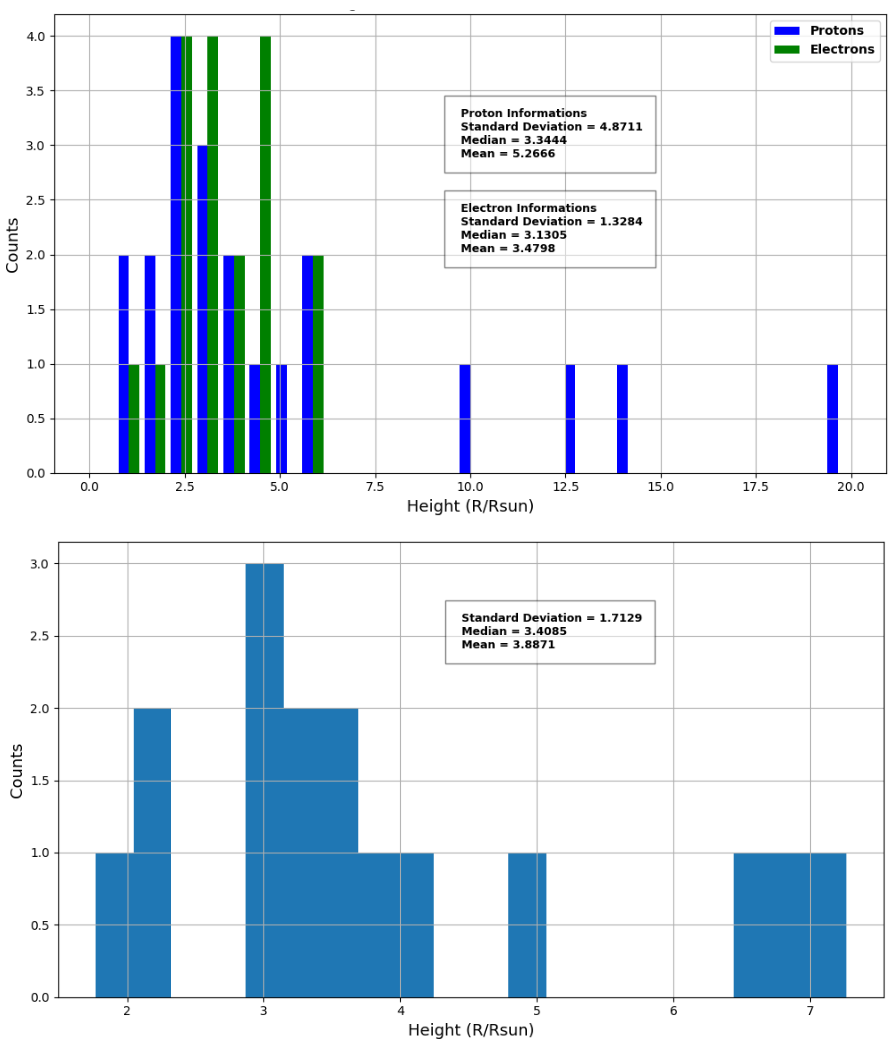

Figure 14. The histograms show the height of the CME at the moment of proton and electron release (left) and at the moment of detection of type II radio emissions (right). The mean, median, and standard deviation of each set are shown within the histograms. The X axis is divided into 20 bins with units R/R_s, and the Y axis reflects the number of events that take a value within each bin.

4. Discussion & Conclusions

For this study, we initially investigated 176 solar energetic particle events with a focus on the relationships between the particle release times, type II and type III radio bursts, and the properties characterizing the associated CMEs and solar flares. From the initially considered set, we ended up with 21 events whose generated results for times $T_{e,rel}$ and $T_{p,rel}$ and for lengths L_e and L_p were found to be within the naturally acceptable values (see all of the related results tabulated in Appendix A). Based on the aforementioned times and their errors, we categorized the events into simultaneous and delayed, and we concluded that 13 (13/21, 62%) were characterized by synchronous particle initiation, while in the remaining 8 (8/21, 38%), either protons or electrons were released later. In particular, in five events (5/21, 24%) the protons were released later than the electrons, and in three events, (3/21, 14%) the electrons were injected into space at a later time than the protons. At the same time, we were able to correlate type II radio emissions in 16 (16/21, 76%) events and type III radio emissions in all cases; while also regarding the associated solar flares in 15 (15/21, 71%) SEP events, it was possible to identify their location. The percentage of simultaneous events is comparable to that reported by Ameri et al. [28] at 53%, Kouloumvakos et al. [19] at 50%, and Xie et al. [23] at 70%.

Figures 2 and 3 of Section 3 separate the SEP events into two groups based on the respective Figure presented by [20]. One would expect this grouping to be in agreement with the categorization of the simultaneous and delayed events. Namely, the first group would contain the simultaneous events, while the second group would contain the delayed p^+ events. Nonetheless, such a conclusion is not supported by our results. The reason why we considered that such a mapping was sensible is that the particles of the simultaneous events probably traveled a similar distance in IP space; therefore, they should belong to the first group for which $L_p \approx L_e$, while in the delayed p^+ events, the electrons would have traveled a shorter distance than the protons, thus resulting in $L_p > L_e$, which is a condition that held in the second group. We found that the path lengths traveled by the protons (L_p) and electrons (L_e) in the simultaneous events were equal. However, for the delayed p^+ events, the path length was shorter for the protons than for the electrons. Most likely, this may be explained by an energy and time-dependent acceleration or release of the protons, which is in line with (e.g., [19,23,28]).

The time differences of the electrons and protons release times with respect to the time differences between the proton release times, type III (see Figure 4) onsets, and type II (see Figure 5) onsets were well organized, which is in agreement with [28] (their Figure 5b) but contrary to [19] (their Figure 8), who found no dependence in such time differences. The linear relationship at each Figure implies that the time difference $Dt_{rel} = T_{p,rel} - T_{e,rel}$ increases as a function of the time differences of $T_{p,rel} - T_{typeIII}$ and $T_{p,rel} - T_{typeII}$. Additionally, we found that electrons are released relatively closer (in time) to the type II and III radio emissions. At the same time, the distribution of the events in these plots indicate that simultaneous events exhibit smaller values of the aforementioned time differences, which is in contrast to the delayed events. Expanding on this, Figures 6 and 7 show that electrons were released in close proximity to (or at most 25 min after) the type III onset and relatively close to the type II radio emissions (±25 min), while protons were also detected at quite large values of the Y axis for ($T_{p,rel} - T_{typeIII}$ and $T_{p,rel} - T_{typeII}$). This suggests that protons can start well after the radio emissions. We found that in simultaneous events, the protons and electrons were released very close to the onset of type III and (for the majority of these events) type II radio emissions. Thus, both of the physical phenomena (i.e., solar flares and CME-driven shocks) contribute in these events, thereby suggesting that a shock wave detected low in the corona with a solar flare occurring at the same time coexist. In addition, our findings suggest a late acceleration or release of the protons in delayed events. This could be explained by a simple scenario of protons being accelerated by an emerging CME, which requires higher altitudes that lead to delayed release times. Nonetheless, there are many other factors that may contribute (e.g., the energy dependence of the particles or the contribution from flare-related processes [49]), which makes such a scenario oversimplified.

Since the time intensity profiles of SEPs are dependent on the longitude of the solar flare and/or the CME that causes the particle increase (see, e.g., [50] and the references therein), the time differences as a function of the connection angle were investigated. It was shown that the angle at which the events were connected did not seem to be decisive in distinguishing between simultaneous and delayed events; this is a conclusion that derives from Figures 8–11. Specifically, simultaneous and delayed events were observed along almost the entire $\Delta\Phi$ (X axis), with no possible way of separating them. This behavior is justified if one considers that, in the absence of an optimal magnetic connection to the region where the event takes place, particles (e^- and p^+) will arrive at the observer (i.e., Earth) late. At the same time, in the aforementioned diagrams, it can be seen that, as $|\Delta\Phi|$ increases, the values of the time differences $T_{p,rel} - T_{typeIII}$, $T_{p,rel} - T_{typeII}$, $T_{e,rel} - T_{typeII}$, and $T_{e,rel} - T_{typeIII}$ increase. The increase of these values implies that the particles with a large $|\Delta\Phi|$ are delayed with respect to the type II and III onsets due to the poor magnetic connection and not due to the simultaneous or delayed release of the particles. In contrast, events with optimal magnetic connection ($\Delta\Phi = (-15^o, 15^o)$) appear to have release episodes of protons and electrons that are close to type III and type II bursts.

The release heights of the protons and electrons shown in Figures 12 and 13 demonstrate that the majority of events with good magnetic connection, (i.e., $\phi_{sf} = (45^o, 75^o)$ or $\Delta\Phi = (-15^o, 15^o)$), were characterized by particles being injected into space before the onset of the type II radio emissions and thus before the formulation of a strong shock wave in the interplanetary medium. By extension, the particles of these events are likely to be accelerated by solar-flare-related processes or processes related to the CME initiation and/or a CME-driven shock that was formed low in the corona [2]. Furthermore, the late p^+ events had large $H_{p,rel}$ and $H_{e,rel}$ values, which were in contrast to the late e^- events and simultaneous events, which were characterized by smaller particle release heights. Figure 14 suggests that the release of electrons, compared to protons, seem to occur in the inner corona (i.e., leading to smaller heights) and that the mean (median) CME height at the time of the type II burst agrees well with the mean (median) release height of the electrons. In contrast, the release height of the protons appears to be larger, which further characterized with a larger dispersion. This delay in the release of protons may possibly be explained by, e.g., the longer times needed for the evolving shocks to be intense enough to produce high-energy SEPs after DH type II onsets and by the times needed for the shocks in SEP events with large $\Delta\Phi$ values to reach the magnetic connection footpoint to the observer [23]. However, processes related to particle transport, the particle's injection at the Sun, and instrumental effects can also be involved in producing such features [49].

It should be noted that the analysis presented in this work relied on 21 SEP events in which the protons were temporally associated with the electrons, and meaningful (F)VDA results were obtained. Thus, our sample is statistically limited. Nonetheless, low statistics is a realistic problem of such studies. For example, Krucker and Lin [20] utilized 26 temporarily associated SEP events; Xie et al. [23] utilized 28 such SEP events; Ameri et al. [28] utilized 36 temporarily associated SEP events; and Dresing et al. [49] investigated 33 such SEP events. As demonstrated here above, the results presented in the current work are in agreement with previous studies. Nonetheless, more work and a larger number of events are needed in order to verify (or not verify) the obtained results.

Our results suggest that in simultaneous events, the electron and proton accelerations are closely related to each other. We showed that delayed p^+ events were released high in the corona, presumably in CME-driven shocks. For simultaneous event flare processes, CME-driven shocks formed low in the corona, and processes related to the CME initiation were more plausible. Finally, delayed e^- events were released in lower heights. A possible interpretation of such behavior is that, due to errors in the times $T_{e,rel}$, these SEP events were mistakenly considered as delayed e^- events when in fact those were simultaneous events.

Author Contributions: Conceptualization, V.K. and A.P.; methodology, V.K., A.P. and A.K.; software, V.K.; analysis, V.K., A.P., A.K., I.A.D. and A.A.; data curation, V.K., A.P. and A.K.; writing—original draft preparation, V.K.; writing—review and editing, A.P., A.K., I.A.D. and A.A. All authors have read and agreed to the published version of the manuscript.

Funding: This research received no external funding.

Data Availability Statement: The study made use of the CDAW CME catalogue (https://cdaw.gsfc.nasa.gov/CME_list/). It further incorporates the solar wind parameters taken from the OMNI database (https://omniweb.gsfc.nasa.gov/; [51], accessed on 15 March 2022), soft X-ray measurements of flares from the AFFECTS database (http://193.190.230.139/), and radio emission spectra from (https://secchirh.obspm.fr/). The study further makes use of the lists of type II and type III radio bursts taken from various catalogs (e.g., https://cdaw.gsfc.nasa.gov/CME_list/radio/waves_type2.html and https://www.swsc-journal.org/articles/swsc/olm/2017/01/swsc170028/swsc170028-1-olm.pdf. Particle data were collected by ftp://ftp.estec.esa.int/private/pjiggens/anonymous/SEPEM_RDS_v2-00.zip; SEPEM RDS, https://utu.sepserver.eu/; ACE/EPAM http://sprg.ssl.berkeley.edu/wind3dp/; and the Wind/3DP. All accessed on 20 September 2023.

Acknowledgments: We are thankful to the referees whose constructive comments have significantly improved the manuscript at hand. We used here the CDAW CME catalog (https://cdaw.gsfc.nasa.gov/CME_list/, accessed on 20 September 2023), which is generated and maintained at the CDAW

Data Center by NASA and The Catholic University of America in cooperation with the Naval Research Laboratory. The SOHO is a project of international cooperation between ESA and NASA. We thank the radio monitoring service at the LESIA (Observatoire de Paris) for providing value-added data that were used for this study.The software responsible for the AFFECTS/STAFF database has been developed at the Royal Observatory of Belgium using the programming languages Java, html, and Javascript in combination with a PostGreSql database. The physical quantities for which the data and measurements are included on the STAFF website are ionospheric and geomagnetic indicators, IP magnetic field measurements, sunspot data, etc.

Conflicts of Interest: The authors declare no conflict of interest.

Appendix A. The 21 SEP Events of the Study

Table A1. For each event the, No, Date, associated solar radio emissions, and calculated heights are given.

ID	Event Date	$T_{p,rel}$	δ T_p (min)	$T_{e,rel}$	δ T_e (min)	$H_p(R_s)$	$H_e(R_s)$	$T_{typeIII,start}$	$T_{typeIII,end}$	T_{typeII}	H_{typeII}	ϕ_{sf} (^{o})	$\Delta\Phi$(^{o})
1	9 May1999	18:00	33	18:11	7.66	2.76	3.34	17:54	18:06	Nan	Nan	Nan	Nan
2	27 May 1999	11:14	6.14	10:59	2.39	5.99	3.8	10:36	11:05	10:55	3.22	Nan	Nan
3	11 June 1999	0:35	4.53	0:48	2.52	1.8	2.61	00:40		Nan	Nan	Nan	Nan
4	18 February 2000	9:10	6.95	9:29	0.93	1.27	2.73	9:16	9:25	9:44	3.88	72	5.66
5	22 July 2000	11:39	14.15	11:52	1.41	2.98	4.36	11:27	11:33	11:45	3.61	56	−3.1
6	20 May 2001	6:29	17.76	6:20	5	3.34	2.92	06:10		6:05	2.22	Nan	Nan
7	4 June 2001	16:49	29.66	16:42	2.55	4	3.72	16:22	16:37	Nan	Nan	59	1.17
8	27 January 2002	12:32	16.84	12:45	6.24	3.34	4.62	12:10	12:30	12:49	5.01	Nan	Nan
9	18 August 2002	22:12	10.56	21:43	11	4.33	2.63	21:10	21:20	Nan	Nan	19	−26.08
10	20 August 2002	8:38	27.87	8:41	5	3.57	3.85	8:25	8:30	Nan	Nan	38	−13.99
11	31 May 2003	2:28	11.99	2:33	5	2.2	2.99	2:20	2:40	3:00	7.26	65	32.13
12	9 November 2004	18:50	4.3	17:32	5	19.53	6.08	17:00	17:25	17:35	6.6	51	11.32
13	14 July 2005	11:32	32.58	10:55	10.25	12.81	6.07	10:20	10:40	11:00	6.98	90	39.05
14	22 August 2005	18:09	35.71	17:21	5	14.04	4.2	17:00	17:30	17:15	2.97	65	17.74
15	21 March 2011	2:57	20.08	2:42	5	6.05	4.31	2:17	2:35	2:20	1.77	Nan	Nan
16	2 August 2011	7:07	38.96	6:26	2.42	5.24	2.73	6:03	6:27	6:15	2.05	15	−35.44
17	8 August 2011	18:03	13.03	18:00	1.53	2.12	1.77	17:59		18:10	2.93	61	17.08
18	13 March 2012	17:27	3.98	17:31	1.75	2.13	2.78	17:20	17:42	17:35	3.43	59	13.51
19	20 February 2014	7:29	12.73	7:50	1.62	1.06	2.78	7:38	7:51	8:05	4	43	0.69
20	25 August 2014	17:54	53.17	15:51	5.46	10.25	4.36	14:50	15:25	15:20	2.88	36	−61.41
21	20 September 2015	18:08	11.55	18:01	3	1.78	1.03	17:55	18:20	18:23	3.39	24	−23.7

Table A2. For each event the No, Date, proton VDA results, electron FVDA results, TSA results, and associated soft X-ray flares and CMEs are given.

No	Date	Proton † VDA		Electron * FVDA		Electron ⋆ TSA	SXR			CME (1st obs.)
		UT	(AU)	UT	(AU)	UT	(Peak Time)	(Magnitude)	ϕ_{sf} (^{o})	UT
1	9 May 1999	18:00 ± 33	2.13 ± 0.62	18:11 ± 08	1.76 ± 0.40	18:10 ± 05	18:10	M7.6	Nan (long > 90)	18:28
2	27 May 1999	11:14 ± 06	1.02 ± 0.13	10:59 ± 02	1.20 ± 0.13	10:57 ± 05	Nan	Nan	Nan	11:06
3	11 June 1999	00:35 ± 05	1.35 ± 0.12	00:48 ± 03	1.62 ± 0.13	00:47 ± 05	Nan	Nan	Nan	01:27
4	18 February 2000	09:10 ± 06	1.59 ± 0.17	09:29 ± 01	1.13 ± 0.05	09:21 ± 05	09:23	C1.1	72W	09:54
5	22 July 2000	11:39 ± 14	1.58 ± 0.34	11:52 ± 01	1.56 ± 0.08	11:43 ± 05	11:25	M3.7	56W	11:54
6	**20 May 2001**	06:29 ± 18	1.11 ± 0.44	06:20 ± 01	1.16 ± 0.04	06:17 ± 05	06:30	M6.4	Nan (long > 90)	06:26
7	4 June 2001	16:49 ± 30	1.91 ± 0.58	16:42 ± 03	1.22 ± 0.15	16:28 ± 05	16:26	M3.2	59W	16:30
8	27 January 2002	12:32 ± 17	2.67 ± 0.36	12:45 ± 06	1.23 ± 0.31	12:50 ± 05	Nan	Nan	Nan	12:30
9	18 August 2002	22:12 ± 11	1.69 ± 0.23	21:43 ± 11	1.22 ± 0.54	21:22 ± 05	21:36	M2.2	19W	21:54
10	**20 August 2002**	08:38 ± 28	2.55 ± 0.65	08:41 ± 08	1.12 ± 0.54	08:38 ± 05	08:24	M3.4	38W	08:55
11	**31 May 2003**	02:28 ± 12	1.10 ± 0.37	02:33 ± 02	1.05 ± 0.12	02:28 ± 05	02:21	M9.3	65W	02:30
12	**9 November 2004**	18:50 ± 4	1.96 ± 0.12	17:32 ± 14	1.07 ± 0.84	17:27 ± 05	17:13	M8.9	51W	17:26
13	14 July 2005	11:32 ± 32	2.46 ± 0.67	10:55 ± 10	1.72 ± 0.60	08:36 ± 05	10:21	X1.2	90W	10:54
14	**22 August 2005**	18:09 ± 36	2.41 ± 0.83	17:21 ± 01	1.10 ± 0.04	17:18 ± 05	16:57	M5.6	65W	17:30
15	**21 March 2011**	02:57 ± 20	2.86 ± 0.43	02:42 ± 11	1.12 ± 0.63	03:02 ± 05	Nan	Nan	Nan	02:24
16	2 August 2011	07:07 ± 39	1.82 ± 0.80	06:26 ± 02	1.00 ± 0.14	06:23 ± 05	06:14	M1.4	15W	06:36
17	8 August 2011	18:03 ± 13	1.52 ± 0.30	18:00 ± 02	1.69 ± 0.08	17:59 ± 05	18:06	M3.5	61W	18:12
18	13 March 2012	17:27 ± 4	1.04 ± 0.09	17:31 ± 02	1.30 ± 0.10	17:29 ± 05	17:24	M7.9	59W	17:36
19	20 February 2014	07:29 ± 13	1.62 ± 0.30	07:50 ± 02	1.22 ± 0.08	07:49 ± 05	07:46	M3.0	43W	08:00
20	25 August 2014	17:54 ± 53	2.26 ± 1.02	15:51 ± 05	1.32 ± 0.33	16:08 ± 05	15:02	M2.0	36W	15:36
21	20 September 2015	18:08 ± 12	1.90 ± 0.22	18:01 ± 03	1.36 ± 0.17	17:47 ± 05	17:51	M2.1	24W	18:12

† SEPEMM/RDS, * Wind/3DP, ⋆ ACE/EPAM; bold font indicates events for which TSA was used.

Notes

[1] https://omniweb.gsfc.nasa.gov/, accessed on 20 September 2023

[2] https://cdaw.gsfc.nasa.gov/CME_list/, accessed on 20 September 2023

[3] http://193.190.230.139/, accessed on 20 September 2023

[4] https://cdaw.gsfc.nasa.gov/CME_list/radio/waves_type2.html, accessed on 20 September 2023

[5] available at https://secchirh.obspm.fr/, accessed on 20 September 2023

[6] which follows from the histograms $H_{e,rel}$ and $H_{p,rel}$ in the next section

References

1. Desai, M.; Giacalone, J. Large gradual solar energetic particle events. *Living Rev. Sol. Phys.* **2016**, *13*, 3. [CrossRef] [PubMed]
2. Reames, D.V. *Solar Energetic Particles: A Modern Primer on Understanding Sources, Acceleration and Propagation*; Springer: Berlin/Heidelberg, Germany, 2021.
3. Carley, E.P.; Vilmer, N.; Vourlidas, A. Radio observations of coronal mass ejection initiation and development in the low solar corona. *Front. Astron. Space Sci.* **2020**, *7*, 79. [CrossRef]
4. Cane, H.V.; Richardson, I.G.; von Rosenvinge, T.T. A study of solar energetic particle events of 1997–2006: Their composition and associations. *J. Geophys. Res. (Space Phys.)* **2010**, *115*, A08101. [CrossRef]
5. Papaioannou, A.; Sandberg, I.; Anastasiadis, A.; Kouloumvakos, A.; Georgoulis, M.K.; Tziotziou, K.; Tsiropoula, G.; Jiggens, P.; Hilgers, A. Solar flares, coronal mass ejections and solar energetic particle event characteristics. *J. Space Weather Space Clim.* **2016**, *6*, A42. [CrossRef]
6. Klein, K.L.; Dalla, S. Acceleration and Propagation of Solar Energetic Particles. *Space Sci. Rev.* **2017**, *212*, 1107–1136. [CrossRef]
7. Kahler, S.W. The role of the big flare syndrome in correlations of solar energetic proton fluxes and associated microwave burst parameters. *J. Geophys. Res. Space Phys.* **1982**, *87*, 3439–3448. [CrossRef]
8. Trottet, G.; Samwel, S.; Klein, K.L.; Dudok de Wit, T.; Miteva, R. Statistical Evidence for Contributions of Flares and Coronal Mass Ejections to Major Solar Energetic Particle Events. *Sol. Phys.* **2015**, *290*, 819–839. [CrossRef]
9. Lavasa, E.; Giannopoulos, G.; Papaioannou, A.; Anastasiadis, A.; Daglis, I.A.; Aran, A.; Pacheco, D.; Sanahuja, B. Assessing the Predictability of Solar Energetic Particles with the Use of Machine Learning Techniques. *Sol. Phys.* **2021**, *296*, 107. [CrossRef]
10. Dierckxsens, M.; Tziotziou, K.; Dalla, S.; Patsou, I.; Marsh, M.S.; Crosby, N.B.; Malandraki, O.; Tsiropoula, G. Relationship between Solar Energetic Particles and Properties of Flares and CMEs: Statistical Analysis of Solar Cycle 23 Events. *Sol. Phys.* **2015**, *290*, 841–874. [CrossRef]
11. Kocharov, L.; Omodei, N.; Mishev, A.; Pesce-Rollins, M.; Longo, F.; Yu, S.; Gary, D.E.; Vainio, R.; Usoskin, I. Multiple Sources of Solar High-energy Protons. *Astrophys. J.* **2021**, *915*, 12. [CrossRef]
12. Reid, H.A.S. A review of recent type III imaging spectroscopy. *Front. Astron. Space Sci.* **2020**, *7*, 56. [CrossRef]
13. Klein, K.L. Radio astronomical tools for the study of solar energetic particles I. Correlations and diagnostics of impulsive acceleration and particle propagation. *Front. Astron. Space Sci.* **2021**, *7*, 105. [CrossRef]
14. Klein, K.L. Radio astronomical tools for the study of solar energetic particles II.Time-extended acceleration at subrelativistic and relativistic energies. *Front. Astron. Space Sci.* **2021**, *7*, 93. [CrossRef]
15. Cliver, E.W.; Kahler, S.W.; Reames, D.V. Coronal Shocks and Solar Energetic Proton Events. *Astrophys. J.* **2004**, *605*, 902–910. [CrossRef]
16. Gopalswamy, N. Solar and geospace connections of energetic particle events. *Geophys. Res. Lett.* **2003**, *30*, 8013. [CrossRef]
17. Gopalswamy, N.; Aguilar-Rodriguez, E.; Yashiro, S.; Nunes, S.; Kaiser, M.L.; Howard, R.A. Type II radio bursts and energetic solar eruptions. *J. Geophys. Res. (Space Phys.)* **2005**, *110*, A12S07. [CrossRef]
18. Papaioannou, A.; Kouloumvakos, A.; Mishev, A.; Vainio, R.; Usoskin, I.; Herbst, K.; Rouillard, A.P.; Anastasiadis, A.; Gieseler, J.; Wimmer-Schweingruber, R.; et al. The first ground-level enhancement of solar cycle 25 on 28 October 2021. *Astron. Astrophys.* **2022**, *660*, L5. [CrossRef]
19. Kouloumvakos, A.; Nindos, A.; Valtonen, E.; Alissandrakis, C.; Malandraki, O.; Tsitsipis, P.; Kontogeorgos, A.; Moussas, X.; Hillaris, A. Properties of solar energetic particle events inferred from their associated radio emission. *Astron. Astrophys.* **2015**, *580*, A80. [CrossRef]
20. Krucker, S.; Lin, R. Two classes of solar proton events derived from onset time analysis. *Astrophys. J.* **2000**, *542*, L61. [CrossRef]
21. Lin, R.P.; Anderson, K.A.; Ashford, S.; Carlson, C.; Curtis, D.; Ergun, R.; Larson, D.; McFadden, J.; McCarthy, M.; Parks, G.K.; et al. A Three-Dimensional Plasma and Energetic Particle Investigation for the Wind Spacecraft. *Space Sci. Rev.* **1995**, *71*, 125–153. [CrossRef]
22. Torsti, J.; Valtonen, E.; Lumme, M.; Peltonen, P.; Eronen, T.; Louhola, M.; Riihonen, E.; Schultz, G.; Teittinen, M.; Ahola, K.; et al. Energetic Particle Experiment ERNE. *Sol. Phys.* **1995**, *162*, 505–531. [CrossRef]
23. Xie, H.; Mäkelä, P.; Gopalswamy, N.; St. Cyr, O. Energy dependence of SEP electron and proton onset times. *J. Geophys. Res. Space Phys.* **2016**, *121*, 6168–6183. [CrossRef]

24. Müller-Mellin, R.; Kunow, H.; Fleißner, V.; Pehlke, E.; Rode, E.; Röschmann, N.; Scharmberg, C.; Sierks, H.; Rusznyak, P.; Mckenna-Lawlor, S.; et al. COSTEP - Comprehensive Suprathermal and Energetic Particle Analyser. *Sol. Phys.* **1995**, *162*, 483–504. [CrossRef]
25. Müller-Mellin, R.; Böttcher, S.; Falenski, J.; Rode, E.; Duvet, L.; Sanderson, T.; Butler, B.; Johlander, B.; Smit, H. The Solar Electron and Proton Telescope for the STEREO Mission. *Space Sci. Rev.* **2008**, *136*, 363–389. [CrossRef]
26. von Rosenvinge, T.T.; Reames, D.V.; Baker, R.; Hawk, J.; Nolan, J.T.; Ryan, L.; Shuman, S.; Wortman, K.A.; Mewaldt, R.A.; Cummings, A.C.; et al. The High Energy Telescope for STEREO. *Space Sci. Rev.* **2008**, *136*, 391–435. [CrossRef]
27. Mewaldt, R.A.; Cohen, C.M.S.; Cook, W.R.; Cummings, A.C.; Davis, A.J.; Geier, S.; Kecman, B.; Klemic, J.; Labrador, A.W.; Leske, R.A.; et al. The Low-Energy Telescope (LET) and SEP Central Electronics for the STEREO Mission. *Space Sci. Rev.* **2008**, *136*, 285–362. [CrossRef]
28. Ameri, D.; Valtonen, E.; Pohjolainen, S. Properties of high-energy solar particle events associated with solar radio emissions. *Sol. Phys.* **2019**, *294*, 1–33. [CrossRef]
29. Paassilta, M.; Raukunen, O.; Vainio, R.; Valtonen, E.; Papaioannou, A.; Siipola, R.; Riihonen, E.; Dierckxsens, M.; Crosby, N.; Malandraki, O.; et al. Catalogue of 55–80 MeV solar proton events extending through solar cycles 23 and 24. *J. Space Weather Space Clim.* **2017**, *7*, A14. [CrossRef]
30. Gold, R.E.; Krimigis, S.M.; Hawkins, S. E., III; Haggerty, D.K.; Lohr, D.A.; Fiore, E.; Armstrong, T.P.; Holland, G.; Lanzerotti, L.J. Electron, Proton, and Alpha Monitor on the Advanced Composition Explorer spacecraft. *Space Sci. Rev.* **1998**, *86*, 541–562. [CrossRef]
31. Stone, E.C.; Frandsen, A.M.; Mewaldt, R.A.; Christian, E.R.; Margolies, D.; Ormes, J.F.; Snow, F. The Advanced Composition Explorer. *Space Sci. Rev.* **1998**, *86*, 1–22. [CrossRef]
32. Crosby, N.; Heynderickx, D.; Jiggens, P.; Aran, A.; Sanahuja, B.; Truscott, P.; Lei, F.; Jacobs, C.; Poedts, S.; Gabriel, S.; et al. SEPEM: A tool for statistical modeling the solar energetic particle environment. *Space Weather* **2015**, *13*, 406–426. [CrossRef]
33. Gopalswamy, N.; Yashiro, S.; Michalek, G.; Xie, H.; Mäkelä, P.; Vourlidas, A.; Howard, R.A. A Catalog of Halo Coronal Mass Ejections from SOHO. *Sun Geosph.* **2010**, *5*, 7–16.
34. Brueckner, G.E.; Howard, R.A.; Koomen, M.J.; Korendyke, C.M.; Michels, D.J.; Moses, J.D.; Socker, D.G.; Dere, K.P.; Lamy, P.L.; Llebaria, A.; et al. The Large Angle Spectroscopic Coronagraph (LASCO). *Sol. Phys.* **1995**, *162*, 357–402. [CrossRef]
35. Miteva, R.; Samwel, S.W.; Krupar, V. Solar energetic particles and radio burst emission. *J. Space Weather Space Clim.* **2017**, *7*, A37. [CrossRef]
36. Gopalswamy, N.; Mäkelä, P.; Yashiro, S. A Catalog of Type II radio bursts observed by Wind/WAVES and their Statistical Properties. *Sun Geosph.* **2019**, *14*, 111–121. [CrossRef]
37. Vainio, R.; Valtonen, E.; Heber, B.; Malandraki, O.E.; Papaioannou, A.; Klein, K.L.; Afanasiev, A.; Agueda, N.; Aurass, H.; Battarbee, M.; et al. The first SEPServer event catalogue˜ 68-MeV solar proton events observed at 1 AU in 1996–2010. *J. Space Weather Space Clim.* **2013**, *3*, A12. [CrossRef]
38. Lintunen, J.; Vainio, R. Solar energetic particle event onset as analyzed from simulated data. *Astron. Astrophys.* **2004**, *420*, 343–350. [CrossRef]
39. Tan, L.C.; Malandraki, O.E.; Reames, D.V.; Ng, C.K.; Wang, L.; Patsou, I.; Papaioannou, A. Comparison between path lengths traveled by solar electrons and ions in ground-level enhancement events. *Astrophys. J.* **2013**, *768*, 68. [CrossRef]
40. Kahler, S.; Ragot, B. Near-relativistic electron c/v onset plots. *Astrophys. J.* **2006**, *646*, 634. [CrossRef]
41. Von Rosenvinge, T.; Barbier, L.; Karsch, J.; Liberman, R.; Madden, M.; Nolan, T.; Reames, D.; Ryan, L.; Singh, S.; Trexel, H.; et al. The energetic particles: Acceleration, composition, and transport (EPACT) investigation on the wind spacecraft. *Space Sci. Rev.* **1995**, *71*, 155–206. [CrossRef]
42. Zhao, L.; Li, G.; Zhang, M.; Wang, L.; Moradi, A.; Effenberger, F. Statistical analysis of interplanetary magnetic field path lengths from solar energetic electron events observed by WIND. *Astrophys. J.* **2019**, *878*, 107. [CrossRef]
43. Li, C.; Firoz, K.A.; Sun, L.; Miroshnichenko, L. Electron and proton acceleration during the first ground level enhancement event of solar cycle 24. *Astrophys. J.* **2013**, *770*, 34. [CrossRef]
44. Papaioannou, A.; Souvatzoglou, G.; Paschalis, P.; Gerontidou, M.; Mavromichalaki, H. The First Ground-Level Enhancement of Solar Cycle 24 on 17 May 2012 and Its Real-Time Detection. *Sol. Phys.* **2014**, *289*, 423–436. [CrossRef]
45. Kouloumvakos, A.; Rouillard, A.; Warmuth, A.; Magdalenic, J.; Jebaraj, I.C.; Mann, G.; Vainio, R.; Monstein, C. Coronal Conditions for the Occurrence of Type II Radio Bursts. *Astrophys. J.* **2021**, *913*, 99. [CrossRef]
46. Patsourakos, S.; Vourlidas, A. "Extreme Ultraviolet Waves" are Waves: First Quadrature Observations of an Extreme Ultraviolet Wave from STEREO. *Astrophys. J. Lett.* **2009**, *700*, L182–L186. [CrossRef]
47. Kozarev, K.; Nedal, M.; Miteva, R.; Dechev, M.; Zucca, P. A Multi-Event Study of Early-Stage SEP Acceleration by CME-Driven Shocks—Sun to 1 AU. *Front. Astron. Space Sci.* **2022**, *9*, 801429. [CrossRef]
48. Thakur, N.; Gopalswamy, N.; Xie, H.; Mäkelä, P.; Yashiro, S.; Akiyama, S.; Davila, J. Ground level enhancement in the 2014 January 6 solar energetic particle event. *Astrophys. J. Lett.* **2014**, *790*, L13. [CrossRef]
49. Dresing, N.; Kouloumvakos, A.; Vainio, R.; Rouillard, A. On the Role of Coronal Shocks for Accelerating Solar Energetic Electrons. *Astrophys. J. Lett.* **2022**, *925*, L21. [CrossRef]

50. Cane, H.V.; Lario, D. An Introduction to CMEs and Energetic Particles. *Space Sci. Rev.* **2006**, *123*, 45–56. [CrossRef]
51. Papitashvili, N.; King, J. OMNI Hourly Data, NASA Space Physics Data Facility. 2020. Available online: https://hpde.io/NASA/NumericalData/OMNI/PT1H (accessed on 15 March 2022).